

Copyright

by

David Glenn Lacina

2007

**The Dissertation Committee for David Glenn Lacina certifies this is the approved
version of the following dissertation:**

**Surface Structure and Related Properties of the (100) Surfaces of
Vanadium and Niobium**

Committee:

James L. Erskine, Supervisor

Leonard Kleinman

John Markert

Jack Swift

Alan Campion

Surface Structure and Related Properties of the (100) Surfaces of

Vanadium and Niobium

by

David Glenn Lacina, B.S.; M.S.

Dissertation

Presented to the Faculty of the Graduate School of

The University of Texas at Austin

in Partial Fulfillment

of the Requirements

for the Degree of

Doctor of Philosophy

The University of Texas at Austin

December 2007

Acknowledgements

I would like to acknowledge my parents and my sister for always being supportive in my education and pursuit of a Ph.D.

I would also like to thank my advisor James Erskine for providing an interesting research project and for all the assistance he has given me over the years. I learned many different things while working in his laboratory and it has been an experience I will never forget.

Finally, I would like to thank all of the other professors at Texas Tech University and the University of Texas that taught me physics and helped me in my education.

**Surface Structure and Related Properties of the (100) Surfaces of
Vanadium and Niobium**

Publication No. _____

David Glenn Lacina, PhD.

University of Texas at Austin, 2007

Supervisor: James L. Erskine

This dissertation addresses atomic-level structure and related properties of the (100) surfaces of Vanadium and Niobium. The primary motivation of the surface structure experiments is based on an observation by P.J. Feibelman^[3,4] that ab-initio calculations of surface relaxation (interplanar separation of near-surface planes) exhibit significant and consistent deviation from corresponding experimental relaxation values obtained through LEED crystallography. The deviation is much larger than the accepted accuracy of both the theoretical and experimental techniques. Resolving this dilemma is the primary objective for this systematic investigation of multilayer relaxation at transition metal surfaces.

This research also addresses important secondary issues. Closely related to the surface relaxation issue for Nb(100) are experiments that provide an experimentally-determined structural basis for the “sub-surface valve” model that has been proposed to explain the novel hydrogen uptake kinetics in Niobium. Definitive experiments that address the longstanding search for ferromagnetic order at the surface of V(100) is another important issue.

Table of Contents

List of Figures	viii
List of Tables	ix
I. Introduction	1
II Experimental Methods	4
II.1 Ultra-High Vacuum	5
II.2 Auger Electron Spectroscopy	6
II.3 Crystal Alignment and Ex-Situ Preparation	7
II.4 In-Situ Preparation	10
II.5 Low Energy Electron Diffraction	
– Experimental Technique	12
III Dynamic LEED Analysis	17
III.1 Basic LEED Analysis	17
III.2 Dynamic Analysis with SATLEED	19
IV Overview of Surface Structure Issues	27
IV.1 The Feibelman Issue	27
IV.2 Surface Relaxation Models	28
IV.3 Review of Previous Work	31
IV.4 Hydrogen Uptake Kinetics in Niobium	35
IV.5 Surface Magnetism in V(100)	41
V Temperature-Dependent Multilayer Relaxation of Clean and Hydrogen-Dosed Nb(100)	45
V.1 Introduction	45

V.2	Sample Preparation	46
V.3	LEED Data and Analysis	50
V.4	Clean and Technically Clean Nb(100) Structure	53
V.5	Hydrogen Dosed Nb(100)	59
V.6	Conclusions	63
VI	Multilayer Relaxation and Search for Ferromagnetic Order at the (100) Surface of Bulk Paramagnetic Vanadium	65
VI.1	Introduction	65
VI.2	Experimental Procedures	69
VI.3	LEED Data and Analysis	72
VI.4	Results for Structure Search	75
VI.5	Surface Impurities and Structure Accuracy	78
VI.6	Probe for Surface Magnetism at V(100)	81
VI.7	Conclusions	87
VII	Conclusion	89
	Bibliography	92
	Vita	98

List of Figures

Figure 1. The universal curve of electron mean free path.	5
Figure 2. Schematic of the LEED System.	12
Figure 3. The Ewald sphere construction in LEED.	15
Figure 4. Digitized LEED pattern.	18
Figure 5. Comparison of experimental LEED IV spectra for Nb(100) crystal.	22
Figure 6. Schematic illustration of the Finnis-Heine relaxation process.	28
Figure 7. Summary of the features of the dilute phase model and surface hydride model.	38
Figure 8. The temperature dependence of the “surface valve”.	40
Figure 9. AES peak ratios for oxygen coverages on Nb(100)	47
Figure 10. LEED intensity spectra for technically clean Nb(100)	51
Figure 11. Graphical illustration of chemisorbed oxygen on Nb(100)	57
Figure 12. Side view of Nb(100) lattice with interstitial hydrogen	60
Figure 13. Representative LEED I-V data set for V(100) plotted with multiple-scattering simulations	74
Figure 14. Graphical representation of variations in the determined surface structure of V(100)	77
Figure 15. Values of first-layer relaxation Δ_{12} at V(100) determined by LEED as a function of surface carbon	80
Figure 16. Calibration of polarimeter and evaluation of background	84
Figure 17. Detected signal with magnetic field applied to V(100).	86

List of Tables

Table I. A summary various transition metal surface experimental and theoretical 1st layer relaxations to demonstrate the Feibelman issue.	27
Table II. Comparison of the ratio of dimer bond length to the bulk nearest neighbor distance for various elements.	30
Table III. Summary of relaxation experiments of previous experiments.	35
Table IV. Calculated and measured magnetizations of V(100)	43
Table V. Calculated and measured surface relaxations for Nb(100).	55
Table VI. Multilayer relaxation determined by LEED for Nb(100) at three temperatures	58
Table VII. Temperature-dependent lattice relaxations relative to bulk Nb for clean and hydrogen-dosed Nb(100).	62
Table VIII. Recent values of calculated and measured first and second-layer relaxations of V(100)	66
Table IX. Nonstructural parameters used in multiple-scattering structure searches and final results for V(100)	76
Table X. Summary of relaxation experiments and calculations for Nb(100) and V(100)	91

I INTRODUCTION

This dissertation addresses atomic-level structure and related properties of the (100) surfaces of Vanadium and Niobium. The research is a logical extension of previous work by G. Teeter^[1] and D. Hinson^[2] who studied corresponding properties of other transition metal surfaces: Rh(100), W(110), and Ti(0001). Low-Energy-Electron Diffraction (LEED) experiments supported by multiple-scattering analysis were used to obtain the surface crystal structure.

The primary motivation of the surface structure experiments is based on an observation by P.J. Feibelman^[3,4] that ab-initio calculations of surface relaxation (interplanar separation of near-surface planes) exhibit significant and consistent deviation from corresponding experimental relaxation values obtained through LEED crystallography. The deviation is much larger than the accepted accuracy of both the theoretical and experimental techniques. Resolving this dilemma is the primary objective for this systematic investigation of multilayer relaxation at transition metal surfaces.

The results presented in this dissertation begin to clarify the origin of the multilayer relaxation dilemma in terms of physical effects resulting from low concentrations of surface impurity atoms. Low concentrations of surface impurity atoms affect surface structure. In both cases studied (Nb(100) and V(100)) the best technically-clean surfaces achieved from currently-available single-crystal boules still result in low level (~5%) surface contamination. The only means available for

achieving realistic comparison of LEED structure with ab-initio calculation is based on careful extrapolation of experimental relaxation parameters to a clean surface result. The described experiments achieve meaningful extrapolations of the top-layer relaxation to a clean surface value, which is found to be consistent with the most recent (and presumably the most accurate) ab-initio calculations. A survey of other transition metal surface systems suggests that surface impurities in LEED experimentation account for some of the discrepancies that underlie the “Feibelman issue”.

This research also addresses important secondary issues. Closely related to the surface relaxation issue for Nb(100) are experiments that provide an experimentally-determined structural basis for the “sub-surface valve” model that has been proposed to explain the novel hydrogen uptake kinetics in Niobium. Definitive experiments that address the longstanding search for ferromagnetic order at the surface of V(100) is another important issue. The ferromagnetic order at some transition metal surfaces including V(100) is purported to be a result of lower atomic coordination and favorable structural and electronic properties of a suitably relaxed surface layer.

The dissertation is organized as follows. Chapter 2 briefly outlines the primary experimental tools used to obtain and characterize clean surfaces and determine surface structure. Chapter 3 outlines important features of electron-diffraction analysis used to extract structural information from LEED intensity measurements. Chapter 4 presents a general overview of surface structure data (with

results of ab-initio calculations) that defines the Feibelman issue and a short description of secondary issues associated with surface relaxations including hydrogen chemisorption effects and the possible occurrence of ferromagnetism at the surface of a paramagnetic element. Chapters 5 and 6 detail the experimental results for Nb(100) and V(100) and conclusions are summarized in Chapter 7 with comments on possible future related research.

II EXPERIMENTAL METHODS

The multilayer-relaxation experiments were based on LEED (measurements of diffracted electron intensity) supported with multiple-scattering calculations. Characterization of the surfaces were based on additional electron-based techniques (photoemission spectroscopy, inelastic electron scattering, and Auger electron spectroscopy) to determine surface impurity concentrations. Magnetic properties of V(100) were probed using a magneto-optic technique. Electron spectroscopy techniques in solids are governed by short electron mean free paths that are a function of the electron kinetic energy. The electron mean free path is the average distance an electron travels between inelastic atomic collisions in a solid. The mean free path is approximately 5-10 Angstroms for all metals in the 20-500 eV energy range and increases to ~100 Angstroms at higher and lower electron energies as seen in Figure 1. Short electron mean free paths limit electron penetration depths into a solid. This results in the very high sensitivity of electron-based techniques to surface structure and chemical composition^[5].

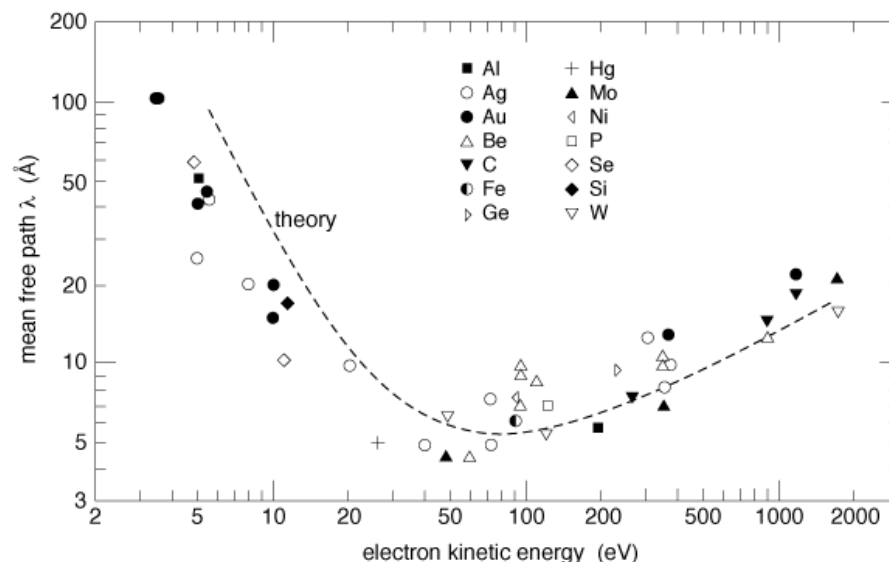


Figure 1. The universal curve of electron mean free path. The theoretical curve of an electron's mean free path over an electron energy range of 0-2000 eV.

II.1 Ultra-High Vacuum

Any experimental technique that is used to probe intrinsic physical properties such as atomic distances, crystal symmetry, or surface roughness (light scattering for example) requires an awareness of how contamination affects the measurement. Relatively low concentrations of reactive surface atoms (H, O, CO) can affect the surface structure^[1]. 10% coverage of H on a metal surface can change the surface relaxation by an amount that is easily detected by a LEED experiment (errors of d_{12} on the 5-10% range have resulted from low 10-20% H surface contamination).

Crystal structure determinations by LEED are based on measurements that can require up to one hour to record raw data. A monolayer of chemisorbed atoms will form on a clean metal substrate (assuming unity sticking probability) from residual

gas at a pressure of 10^{-8} Torr in less than five minutes. Obtaining LEED data from sample surfaces that are acceptably clean for dynamical analysis requires a crystal surface to be free of impurities during experimentation. This requirement limits the upper base pressure of the experimental apparatus to the low 10^{-10} Torr (the ultrahigh vacuum) range. A vacuum system operating in the ultrahigh vacuum range contains primarily residual hydrogen and CO atoms. A monolayer of chemisorbed CO or hydrogen will form on a crystal surface within one hour unless the sample is annealed above the desorption temperature at suitably short time intervals; but annealing can also cause impurity-atom diffusion from the bulk to the surface. Clearly, it is necessary to monitor the surface composition.

II.2 Auger Electron Spectroscopy

The atomic composition of a crystal surface is measured using Auger Electron Spectroscopy (AES). Every atom has a unique set of electron energy levels that can be used to provide atom-specific information about surface composition. AES is a three-electron process in which an incident high-energy electron ionizes an atom core electron state leaving the atom in an ionized state. The atom excited state can transform to a lower energy state by having an electron from a higher-level fill the “hole” left by the ionizing electron. Energy is conserved in this process by the atom emitting an electron (Auger process) or by fluorescence (which is less favorable in higher Z atoms). The kinetic energy of the Auger electron is characteristic of the atom from which it was emitted. The intensity of emitted Auger electrons is proportional to the concentration of atoms; therefore AES is an atomic sensitive

quantitative tool for surface compositional analysis. AES spectroscopy is capable of achieving sensitivity of 1 percent atomic surface coverage.

A perfectly clean crystal surface (characterized by AES) exhibits no detectable impurities, suggesting a surface concentration below 1%. However, AES is unable to detect any atoms with less than three electrons (hydrogen and helium). Helium is not an issue because it is inert and occurs in vanishing small concentrations in UHV systems, but hydrogen contamination can be a major problem for any experiment related to surface structure or interlayer relaxations. Experiments involving hydrogen atoms require a complementary technique (electron energy loss spectroscopy)^[6-8] to determine the concentration of hydrogen at the crystal surface. AES is further limited by short electron mean free paths, and can not be used to directly monitor impurities in a crystal beyond the near-surface region.

II.3 Crystal Alignment and Ex-situ Preparation

Single crystal metal boules can be purchased from various suppliers. The boules are typically about 10mm in diameter, a few inches long, and are grown with the boule axis along a specific crystallographic axis. The purity (resulting from zone refining during the growth process) can be as high as 99.9995% or better, but with $\sim 10^{23}$ atoms/cm³, there are approximately 10^{18} impurity atoms/cm³ which generally tend to migrate to the surface during in-situ cleaning (annealing).

X-ray diffraction is the standard technique for determining crystal structure of single crystal boules^[9]. The Laue method^[10] applied to x-ray diffraction is a very convenient technique for rapid determination of crystal alignment and symmetry of

single crystal boules or prepared oriented samples. The alignment phase of the sample preparation process is based on the x-ray Laue method assisted by OrientExpress software described later.

The single crystal boule is held by a special goniometer in a stationary beam of collimated x-rays. The goniometer allows a boule or a cut sample to be rotated around two orthogonal axes, providing a means of adjusting the crystallographic orientation. The Laue method utilizes the continuum (white) radiation from an x-ray tube (wavelength ranges from few tenths to a few angstroms). Each lattice plane of the crystal selects from the incident beam a wavelength that satisfies Bragg's condition: $2d \sin \Theta = n \lambda$. Constructive interference conditions result in high intensity points on a photograph which when developed yield the Laue pattern of diffracted x-rays.

OrientExpress^[11] is a (public domain) software package that was developed to facilitate crystal alignment based on flat-plane Laue pattern photographs scanned into a personal computer. Basic crystal parameters are input into OrientExpress (lattice constant, symmetry) along with x-ray source parameters (film to crystal distance x and continuum wavelength range). OrientExpress solves the Laue equations for a prescribed crystal orientation (in which case it presents a stereographic projection of the diffraction pattern), or the user can identify a number of diffraction peaks on the digitized Laue pattern and OrientExpress will provide the orientation angles in relation to a specified crystallographic axis.

Aligned samples are cut from single crystal boules using an Electric Discharge Milling (EDM) machine. The EDM machine can cut any metal crystal with a minimum of surface damage. The EDM machine allows a crystal or boule mounted in the special goniometer to be cut and still maintain the crystal alignment determined with the X-ray Laue method. Commercially-polished, pre-aligned silicon(111) crystals ($.01^\circ$ accuracy) are used for instrument calibration and alignment.

The EDM machine is equipped with a track that allows a crystal or boule mounted in the goniometer to be transferred to the EDM machine for the cutting phase while preserving the alignment determined by the X-ray Laue method. Our EDM machine uses a moving-wire electrode to cut crystals. The alignment accuracy of an EDM cut depends on the wire-cutter plane being perpendicular to the EDM track axis. This assumes that the x-ray track axis is parallel to the collimated x-ray beam.

Accurate alignment of the crystal sample prior to the cutting phase of crystal preparation reduces the amount of material that must be removed during the polishing/final alignment phase. Additionally, all metal boule cutting techniques result in sample surface damage, but correct polishing procedures can create a high-quality crystal surface. The precision alignment required for LEED crystallography experiments is accomplished during the polishing phase of crystal preparation.

A cut crystal sample is mounted on a stainless steel polishing jig for surface polishing. The polishing jig allows the sample to be adjusted within 0.5° of any desired crystallographic orientation based on Laue techniques. The grinding and

polishing of crystals is carried out in two steps: the first step produces accurate alignment and uniform sample shape and thickness for in-situ mounting; the final step is to polish away as much surface damage as possible.

Accurate alignment of a cut crystal is determined through X-ray Laue diffraction of the mounted sample. Uniform sample width is produced by grinding a sample surface oriented along a desired crystallographic axis with coarse grit sandpaper. The first step of polishing can be completed quickly and produces an aligned sample with parallel crystal surface faces, but significant surface damage (deep scratches) is present.

The final step of crystal polishing is accomplished through repeated cycles of lapping the crystal surface with polishing compounds constantly reducing the grit size. The polishing compounds can be either alumina (Al_2O_3) or diamond abrasives with grit sizes varying from 40 μm to 0.05 μm . The length of time spent polishing the crystal at one grit size before moving to a finer grit size differs for each type of sample material. The exact polishing procedure to create a polished crystal surface is a matter of trial and error but is described in some detail in my MS thesis^[12]. A finished polished crystal will have a mirror like surface with no visible surface damage.

II.4 In-Situ Preparation

Before any meaningful surface analysis or related experimental work is possible with a new crystal, bulk impurities must be removed from the surface region of a crystal. Ion beam milling is capable of removing the surface atoms of a sample,

revealing the atomic layers immediately below. Ion beam milling facilitates the removal of elemental impurities, provided the impurities can be concentrated at the surface by thermally-activated diffusion. Typically, neon gas is chosen for ion beam milling since it does not adsorb in titanium sublimation pumps at 77°K as other noble gasses (argon) are known to do. Electron beam heating (annealing) is used to raise the sample to the high temperatures require to promote diffusion of impurities to the sample surface. High-temperature annealing also allows the surface atoms to recover crystal order after being damaged through ion beam milling.

A combination of ion beam milling and e-beam heating is the most effective method of removing near-surface impurities from a sample. The specific procedures used to clean Nb(100) and V(100) are described in Chapters 5 and 6 respectively. A balance needs to be maintained between the milling rate and the diffusion rate to achieve a reduction in the near-surface bulk impurity concentration and to achieve a low surface impurity concentration. Restoring crystal order to a sample surface can be done through annealing or flashing. Flashing is e-beam heating at a very high temperature for only a few seconds; the short time interval is necessary to avoid diffusion of impurities to the surface. The sample temperature is monitored during flashing the sample to avoid surface damage from local melting.

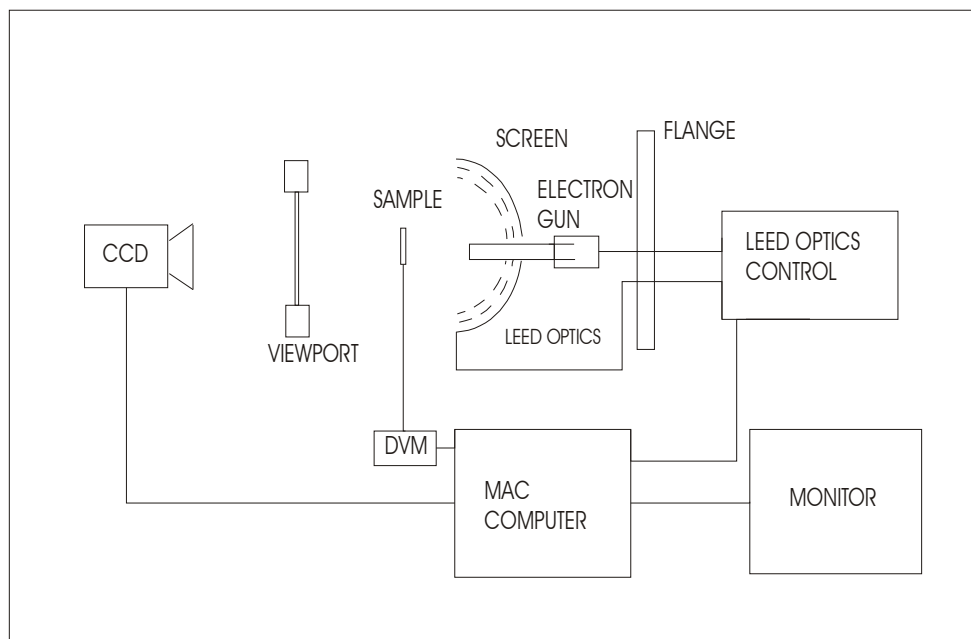


Figure 2. Schematic of the LEED System. This schematic includes LEED optics used in production of a LEED pattern, CCD camera that records real-time images of the LEED pattern, the computer that records LEED pattern data, and the target current monitor.

II.5 Low Energy Electron Diffraction – Experimental Technique

Our LEED measurements were carried out using commercial display-type optics, as shown in figure 2. This instrument consists of an electron gun that directs a nearly monochromatic beam of low energy electrons (20-1000 eV energy range) at a sample in combination with a set of spherical grids and fluorescent screens to detect the diffracted electron beams. The sample is located at the center of the concentric screen (which is also the focal point of the electron gun) and is oriented with the surface-normal parallel to the gun axis. Four grids are used to filter scattered electron energies (high-pass filter) and provide a (electric) field-free region between the sample and the first grid. The gun acceleration voltages and retarding grid voltage

are ramped together to sweep the kinetic energy of diffracted electrons. The computer provides a timed linear voltage ramp output that drives the LEED optics control electronics.

The electron diffraction patterns, including the intensity of the diffracted electron beams as a function of kinetic energy, are captured by a CCD camera interfaced to the computer via a standard frame-grabbing card. The camera sensitivity can be adjusted to take full advantage of its dynamic range for a prescribed range of fluorescent spot intensity. Software and macro programs permit automated capture of LEED frames, beam tracking, and intensity determination of the LEED spots.

Low Energy Electron Diffraction provides an excellent method for making fine adjustments in the crystal alignment, confirming the quality of a prepared crystal surface, and for determining atomic-scale structural information (multilayer relaxation) of a crystal surface in the near-surface region. An incident electron beam diffracts from a crystal surface in a limited number of directions that are determined by Laue conditions. The very short mean free path of low energy electrons limits the effect of the out-of-plane (third) Laue condition leading to a diffraction pattern dominated by a two-dimensional character.

The in-plane Laue conditions result in the symmetry of the surface unit cell being manifested by in the diffraction pattern. A crystal that is not properly aligned will have an asymmetric diffraction pattern. Any impurities or damage to a crystal surface alters the quality of the diffraction pattern (diffuse diffraction spots) and

ordered impurity layers or ordered surface reconstruction can produce LEED patterns having different symmetry than a clean surface. Multiple scattering of an electron within the top atomic surface layers produces variations in the intensity (I) of the diffracted beams as a function of kinetic energy (V). Three-dimensional information, such as interlayer spacings, are extracted from LEED I-V graphs.

Ewald sphere construction allows a graphical means of determining the diffracted beam angles for specific crystal geometries. For low energy electron diffraction, the three-dimensional reciprocal lattice is replaced by two-dimensional lattice rods resulting from the limited third Laue condition. Figure 3 shows a typical Ewald sphere construction viewed in a two dimensional projection along a specific $k_{||}$ direction.

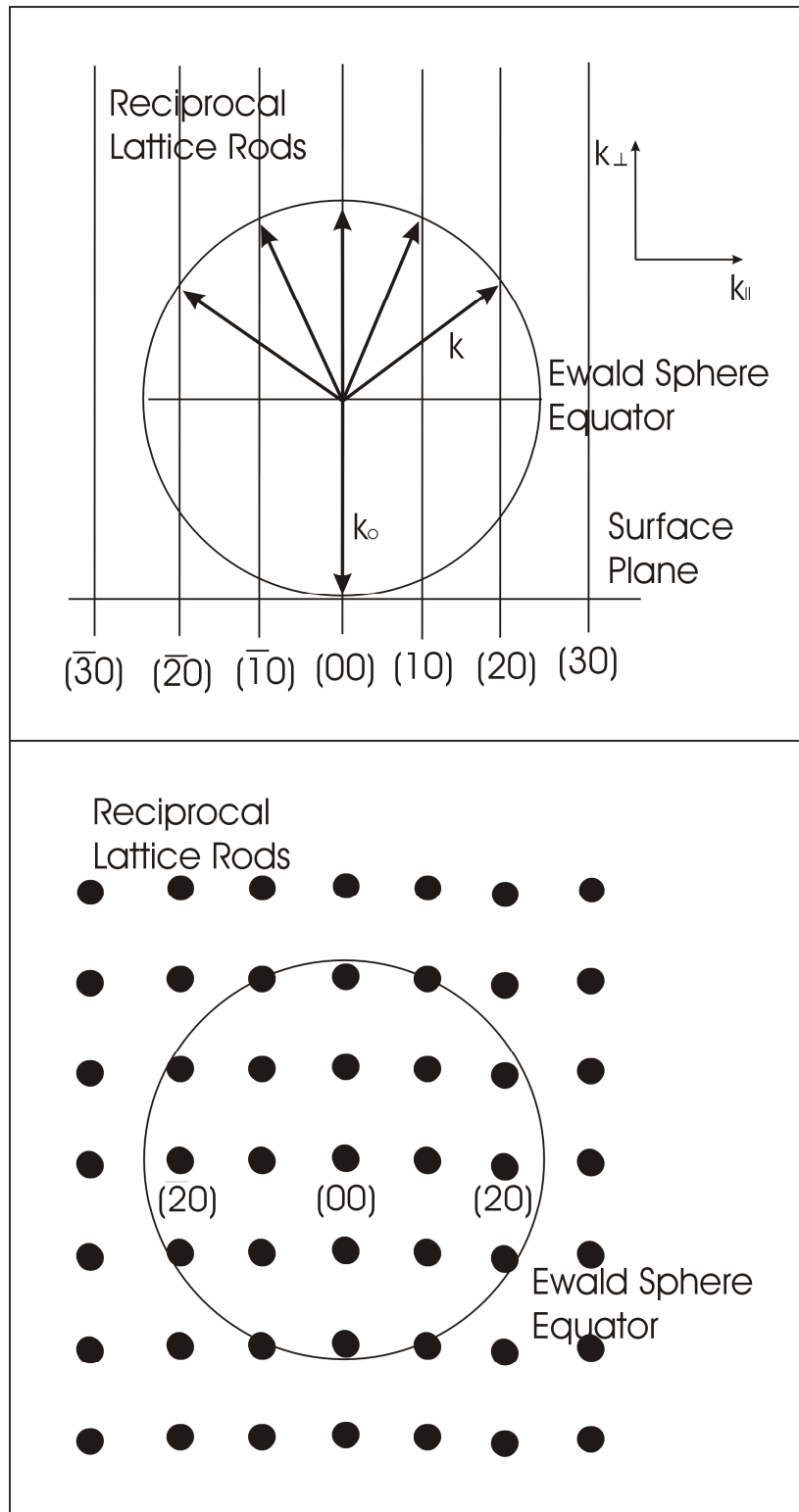


Figure 3. The Ewald sphere construction in LEED. The Ewald sphere is shown at a single energy from the same incident direction: (a) view parallel to the surface, and (b) view perpendicular to the surface showing the equator of the ewald sphere.

Ewald sphere construction requires satisfaction of the following scattering conditions: momentum transfer parallel to the surface must be a single reciprocal lattice vector, and energy must be conserved. Parallel momentum transfer is represented graphically in reciprocal space by the condition that a reflection (k) will only occur when a reciprocal lattice rod falls on the sphere, the center of which is at the origin of k_0 . The energy of the electron scattering is conserved if the scattering is elastic. Represented graphically, the magnitudes of the diffracted beam wavevector k must be equal to the magnitude of the incident beam wavevector k_0 .

As the incident electron energy increases, the radius of the Ewald sphere increases. The diffracted beams observed on a LEED fluorescent screen will change position as they move toward the center while new beams appear at the screen edge. This occurs as the Ewald sphere expands and intersects new lattice rods.

III DYNAMIC LEED ANALYSIS

III.1 Basic LEED Analysis

Basic LEED analysis is defined as visual interpretation of the diffraction pattern to determine structure-related properties. LEED diffraction patterns are representative of crystal surface structure and unit cell symmetry. Clean Nb(100) and V(100) (both bcc metals) have unreconstructed surfaces, consequently their diffraction patterns are a simple manifestation of the bulk unit cell symmetry oriented along a specific crystallographic direction. The Ewald sphere construction supported by knowledge of crystal symmetry and orientation reproduces the LEED diffraction pattern. Figure 4 is a photograph showing the diffraction pattern for a V(100) crystal.

Visual analysis of a diffraction pattern confirms the preparation of a crystal surface by judging the quality of the diffraction spots. Well-ordered crystal surfaces diffract the incoming electron beam according to Bragg's law producing a sharp, well-defined pattern of diffraction spots surrounded by a dark background. A disordered crystal surface will diffract incoming electrons generously creating a pattern with broad, fuzzy diffraction spots surrounded by a bright background. A crystal surface that is completely disordered, or is covered by surface impurities, will produce a bright background with no visible diffraction pattern. Auger electron spectroscopy and visual diffraction pattern analysis are the most effective methods for confirming crystal quality and monitoring the progress of in-situ cleaning.

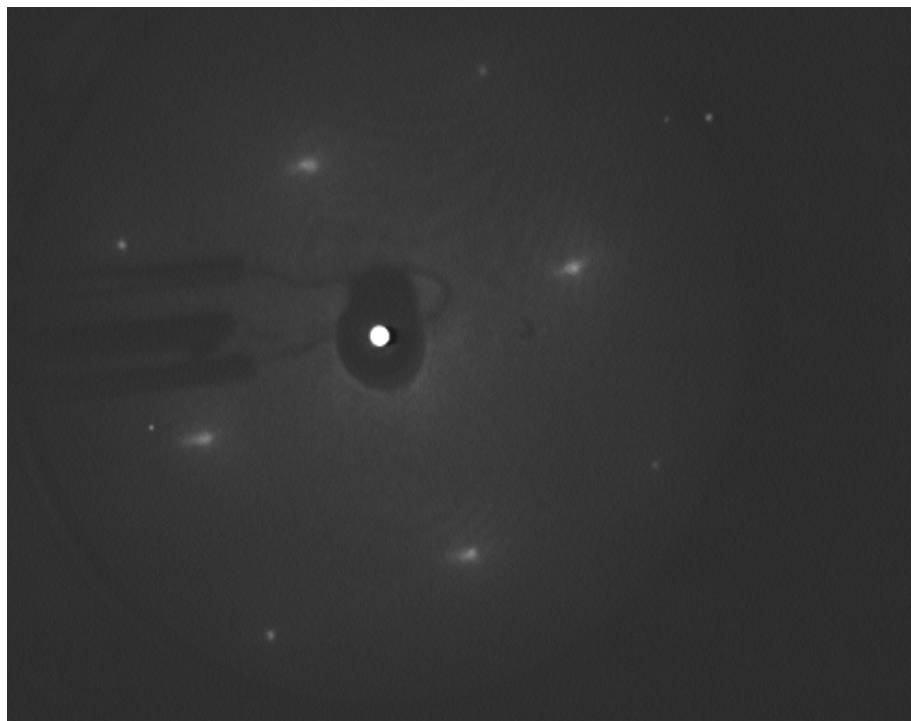


Figure 4. Digitized LEED pattern. This LEED pattern was produced by V(100) crystal at 100 eV. The in-phase beams (outer four spots) are sharp, and the background is low indicating a clean surface and that the sample is rotated 15° counter-clockwise. This rotation has no effect on conjugate beam symmetry.

LEED crystallography requires measurement of the intensity of the diffraction pattern spots as a function of the incoming electron kinetic energy. The multiple scattering calculations that lead to structural information require orientation of the crystal precisely perpendicular (normal) to the incoming electron beam. A crystal precisely oriented along a crystallographic axis generates, as a result of Bragg's law, separate diffracted beams of equal intensity that vary as a function of the electron kinetic energy. These separate diffracted beams are symmetry-degenerate and of the same Bragg order. Figure 4 displays an example of four first-order spots and four

second-order spots. Equivalence of the symmetry-degenerate spot intensities for a positioned crystal confirms the success of the in-situ alignment phase of the experiment. Details regarding visual LEED analysis of unusual crystal surfaces (surface reconstructions, ordered overlayers, vicinal surfaces, etc.) can be found in the dissertation by G. Teeter^[1].

III.2 LEED Analysis with SATLEED

Obtaining multi-layer relaxations, and more general three-dimensional surface structure information (surface reconstruction) from a crystal using low-energy-electron diffraction requires computational analysis of LEED I-V graphs. The Van Hove\Barbieri SATLEED program^[13] calculates theoretical IV spectra based upon a user input reference structure. Experimental and theoretical I-V spectra are tested for compatibility using expressions that define r-factors that quantitatively describe the compatibility. Structural and non-structural parameters that physically describe the reference structure are altered until the compatibility, as determined by r-factors, is high. The degree of compatibility can also be used to determine the error associated with a LEED experiment. A high experiment-theory compatibility that requires a physically impossible reference structure (excessive interlayer relaxations) indicates large errors in the experimental spectra. Error associated with the theoretical spectra can be minimized by careful attention to reference structure parameters and methodology including starting parameters and search range limits.

There are different r-factor equations that stress different features of the I-V curves, and more than one r-factor is employed to calculate the comparison. A low r-

factor number indicates excellent experiment-theory compatibility. Two of the most widely-used r-factors in LEED crystallography are the Pendry r-factor, R_p ,^[14] and the Zanazzi-Jona r-factor^[15]

Zanazzi-Jona uses a combination of first and second derivatives and emphasizes peak positions, positions of peak maxima and minima, and takes into account the curvature of the spectra. The Zanazzi-Jona is defined by:

$$R_{ZJ} = A_{RZJ} \int [|I_e'' - cI_t''| |I_e' - cI_t'| / (|I_e'| + \max|I_t'|)] dE$$

where A_{RZJ} is a normalization factor used to eliminate dimension from the r-factor integration; I' and I'' are the first and second derivatives of the peak intensity. This method matches peak placement when comparing two I-V curves, the best r-factors for this method are returned when peaks from two curves match at the same energy with little importance on the curves shape.

In all r-factor formulae other than the Pendry r-factor, the peaks are weighted in proportion to their heights. The Pendry r-factor evaluates all peaks with equal weight. Overlapping peaks are not treated equally if they have different heights.

$$R_p = \int (Y_e - Y_t)^2 dE / \int (Y_e^2 - Y_t^2) dE \quad Y = (I'/I) / (1 + V_{oi}^2 (I'/I)^2)$$

Y_e and Y_t are intensity functions representing experiment and theory I-V curve data, respectively. I'/I is the logarithmic derivative of peak intensity and V_{oi} is the average peak width of individual peaks as opposed to peaks that overlap in the I-V curves. The Pendry r-factor is widely accepted as the most accurate criteria of compatibility. The Van Hove\Barbieri SATLEED program allows the use of ten

different r-factors in determining experiment-theory compatibility, but only the two r-factors described here (Zanazzi-Jona and Pendry) were used during SATLEED analysis.

R-factor analysis is also an effective method for determining the internal consistency of experimental data prior to SATLEED analysis. Testing the quality of experimental data is accomplished through r-factor comparisons of the symmetry-degenerate beam I-V curves (described in the previous section). Figure 5 is an example this type of analysis. R-factor equations can also be used to evaluate the compatibility of symmetry-degenerate beams from independent experimental datasets to confirm the accuracy of experimental methodology. The availability of digitized experimental data published by other groups allows r-factor analysis to be used to compare independently-measured I-V spectra sets and confirm the accuracy of experiments conducted by different groups. The Igor Pro software program is used to perform the R-factor analysis in all the preceding calculations.

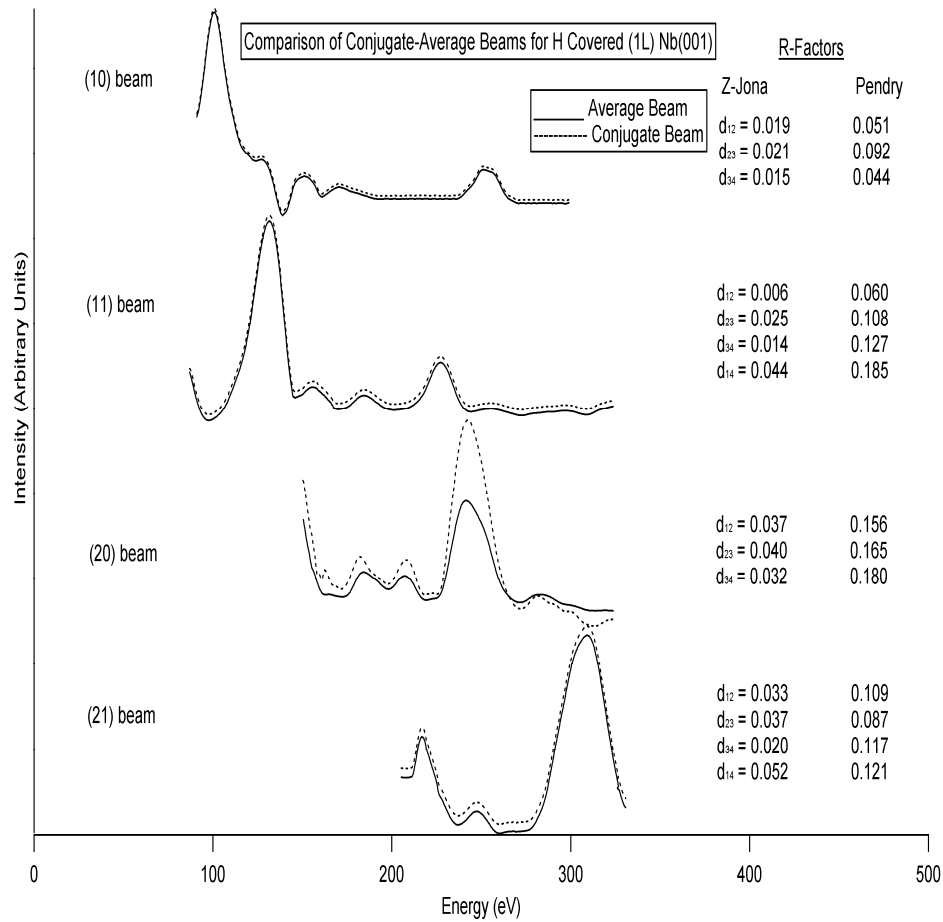


Figure 5. Comparison of experimental LEED IV spectra for Nb(100) crystal. The R-factors displayed (Pendry and Zannazi-Jona) characterize the level of agreement between the individual conjugate beams and the beam averaged from all four conjugate beams. The low R-factors indicate excellent agreement for this data.

Constructive interference of scattered electrons from the surface atomic layers cause the intensity variations present in experimental I-V curve graphs. The Van Hove multiple scattering code numerically calculates this interference based on a reference crystal structure, and also includes the scattering effects associated with a single atom. The SATLEED program uses pre-calculated phase shifts in the

reference structure to account for the single atom scattering processes. Phase shifts describe the electron scattering from a single atom through Fourier transforms applied to the atomic potential for each element in the reference structure.

Phase shifts are calculated using the Van Hove/Barbieri phase shift package. This package consists of four programs that are used to produce the phase shift information needed to complete a SATLEED reference structure. The programs calculate the following for each element in the reference structure: self-consistent orbitals, the total radial charge density, the muffin tin potential, and finally the phase shifts. Phase shifts are automatically formatted for inclusion into the reference structure input files. The phase shift package requires a basic reference structure to produce accurate phase shifts, but phase shifts are not sensitive to the input structure. Therefore, incorrect structural data will not alter the calculated phase shifts significantly.

Another important parameter that can significantly affect surface structure computations is the inner potential. The inner potential describes the electrostatic potential difference between vacuum and inside the crystal surface as well as the effects caused by short electron mean free paths. The SATLEED program accounts for the inner potential through a parameter (V_o) separated into real and imaginary parts. The real part of the potential (V_{or}) accounts for the energy shift of the electrons as they cross into the crystal surface, being accelerated by the electrostatic potential difference. The imaginary part (V_{oi}) is a numerical representation of the inelastic scattering an electron experiences near the surface that characterizes the electron

mean free path. The real part of the inner potential is adjusted automatically by the SATLEED program as it performs a structure analysis with an optimum value produced as a final result. The imaginary part of the inner potential is manually entered as a variable in the program.

The input files used by the SATLEED program to compute an experiment-theory IV curve comparison consist of the following: experimental IV curve data, a file selecting specific r-factors and the degree of data smoothing, the theoretical reference structure, and the base values for all structural parameters (listing the exact parameters that are to be varied during calculation). The non-structural parameters present in the reference structure are the real and imaginary parts of the inner potential, Debye temperatures, vibrational effect amplitudes, atomic mass data, and phase shift information. Structural parameters are input as a bulk structure (not varied during calculation) covered by a number of surface composite layers. The surface composite layers and related information, such as the exact number of layers, atomic distances, crystal unit cells, etc., are the primary variables in the SATLEED computation.

The procedure for a structure search is a two-step process that consists of running two SATLEED programs. The first program computes theoretical LEED intensities for the diffracted beams that were measured experimentally. Additionally, the first program calculates tensors that allow the computation of the theory-experiment comparison in the second program. The second program varies the atomic positions of the reference structure atoms, computes LEED intensities based

on the modified positions, compares these intensities with experimental IV data, updates the atomic positions based on the results of comparison, and iterates until the process converges to an optimum r-factor value. The r-factors that quantify the theory-experiment computation are minimized during convergence.

The output of the SATLEED program includes the following: theoretical IV curves, experimental IV curves, best-fit structural parameters, optimum r-factors, and an ideal inner potential value. IV curves, in the form of smoothed theoretical and experimental curve data, are listed in different output files specified by individual conjugate beam. Smoothed theoretical and experimental curves are used in the SATLEED program, but the degree of smoothing is minimized to maintain the accuracy of the structural calculations. The best-fit structural parameters consist of new atomic positions for the reference structure.

A structure search is completed when the structural and non-structural parameters have been refined to produce a consistent surface structure with the lowest calculated r-factors. An iterative process involving repetition of the two previously outlined programs refines the structural parameters of a computation. The calculated best-fit structural parameters are placed into the reference structure and the SATLEED program is run, producing new best-fit structural parameters. This replacement process continues until the calculated best-fit structure is equivalent to the reference structure. Once the structural parameters have been optimized, the non-structural parameters are refined. The non-structural parameters are varied one at a time followed by the iterative structural parameter process. This structure search

procedure allows the optimization of the structural and non-structural parameters while minimizing the r-factors.

The statistical error for structural parameter calculations using the Pendry r-factor is estimated by the variance equation: $\text{var}(r_p) = r_{\min} \sqrt{(8|V_{oi}|/\Delta E)^{[14]}}$. r_{\min} is the minimum Pendry r-factor produced by the SATLEED calculations, V_{oi} is the imaginary part of the inner potential, and ΔE is the overall energy range of the experimental data. The variance equation indicates that statistical error will be high if the energy range is short or if the sample surface is contaminated (the inner potential is larger when impurities are present on a crystal surface). Studies by G. Teeter show that a total energy range of 1200 eV (for four non-equivalent beams) is generally sufficient to produce reliable structure results and to eliminate the error associated with SATLEED calculations. A range of 1000 eV is sufficient to avoid any significant variations due to computational error^[1].

IV Overview of Structural Issues

IV.1 The Feibelman Issue

The Feibelman issue is defined as the consistent discrepancy between interlayer relaxation measurements and ab-initio calculations for certain transition metal surfaces. Ab-initio calculations predict multilayer relaxations that are 2-5 times greater than experimental measurements. The experiment-theory discrepancy is beyond the error that can be attributed to experimental methodology or theoretical calculations. Table I illustrates the Feibelman issue through currently known experimental and theoretical relaxation values for various transition metals^[4].

$\Delta d_{12}/d_0$		
Surface	Experiment	Theory
Ti(0001)	-4.9%	-7.7%
Zr(0001)	-1%,-1.6%	-6.3%,-4.4%
Mo(110)	-1.6%	-3.9%,-4.5%
Rh(001)	-1.4%	-3.5%,-5.1%
Ru(0001)	-2%	-4%
W(110)	-3%, -1.3%	-3.3%

Table I. A summary of the experimental and theoretical 1st layer relaxations of various transition metal surfaces that demonstrates the Feibelman issue. The experiment-theory discrepancy for the W(110) surface has been resolved by a recent experiment (ref 1).

IV.2 Surface Relaxation Models

The Finnis-Heine model^[16] is a conceptual model that attempts to account for trends found in experimental measurements of top-layer relaxations. The Finnis-Heine model states that the surface atomic layer of a cut crystal experiences Smoluchowski charge-smoothing^[17] in order to lower the potential energy of the atoms in a surface layer. The electrons in the surface atomic layer are assumed to redistribute to lower their total kinetic energy by moving to fill the empty spaces between the atomic cores. This behavior causes a small contraction of the first atomic layer that is a universal trend for all elements.

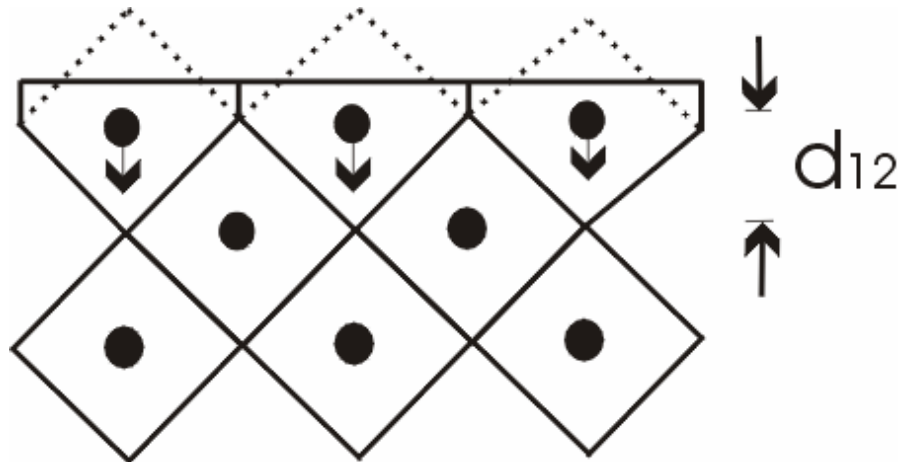


Figure 6. Schematic illustration of the Finnis-Heine surface relaxation process^[4]. The black dots represent atomic ion cores, with the solid\dashed lines representing the charge distribution after\before charge smoothing.

The Finnis-Heine model accounts for trends in relaxations for many metal surfaces, but transition metal surfaces do not follow Finnis-Heine model predictions. Flaws of the Finnis-Heine model include an inability to explain surface layer

expansions, the inability to explain differing degrees of relaxation for similar crystallographic faces of different crystals, and a failure to explain large contractions >10%. Recent experiments report a surface layer expansion of 6% for both Mg(0001)^[18,19] and Be(0001)^[20,21] that can not be explained by the Finnis-Heine model. Another multilayer relaxation experiment researching the Ta(100) surface reports a large surface contraction of 14%^[22].

Feibelman developed a new model that attempts to account for surface relaxation trends based on chemical bonding arguments. The new model is the promotion-hybridization model and is based on bond order changes resulting from the termination of the crystal surface. The valence electrons of a surface atom that would have bonded with atoms in the next bulk layer must, due to the lattice termination at the surface, re-hybridize into more energetically-favorable states. The most favorable states typically result in the shortening of bonds between the surface and near-surface atoms.

The expansion or contraction of the first surface layer is governed by the ratio of the dimer bond length to the nearest neighbor distance. Expansion of the surface occurs if this ratio is greater than one, and contraction occurs if it is less than one. Large relaxations occur if there is a significant difference between the dimer bond length and nearest neighbor distance. Table II lists dimer bond lengths, nearest neighbor distances, and their ratio^[4] for different elements.

Element	Group	R_{dimer}	R_{nn}	$R_{\text{dimer}}/R_{\text{nn}}$
Li	IA	5.05	5.71	0.88
Na	IA	5.82	6.91	0.84
K	IA	7.38	8.55	0.86
Be	IIA	4.66	4.20	1.11
Mg	IIA	7.35	6.05	1.22
Al	IIIA	5.10	5.40	0.95
Bi	VA	5.03	5.80	0.88
Cu	IB	4.20	4.84	0.87
Ag	IB	4.78	5.46	0.88
Au	IB	4.67	5.44	0.86
Zn	IIB	7.56	5.03	1.50
Cd	IIB	9.10	5.63	1.62
Hg	IIB	6.86	5.69	1.21
Ti	IVB	3.67	5.46	0.67
Zr	IVB	4.25	5.99	0.71
V	VB	2.99	4.95	0.60
Mo	VIB	3.66	5.14	0.71
Fe	VIII	3.82	4.69	0.81
Ni	VIII	4.07	4.71	0.86

Table II. Comparison of the ratio of dimer bond length to the bulk nearest neighbor distance for various elements. If this ratio is less than one the surface layer will contract. The source is listed in reference 4.

The promotion-hybridization model provides a simple method to attempt a general understanding of transition metal surface relaxations, but there are flaws with this model as well. For example, an experiment on Be(0001) shows a large surface

expansion^[21]. As a result of this experiment, the promotion-hybridization model predicts Be(1010) should exhibit a larger expansion than Be(0001). Be(1010) surface relaxation experiments verify a contraction, not expansion, of the surface atomic layer proving the promotion-hybridization model predictions are incorrect.

The primary cause of the Feibelman issue might originate from experimental methodology rather than from the limited accuracy of simple models and ab-initio calculations for predicting top-layer relaxation. Hydrogen contamination can produce large changes in surface-layer relaxations, but few experiments monitor hydrogen during multilayer-relaxation measurements. Defects in crystal surfaces, such as structural defects, strain, or disordered surfaces, could affect the relaxation of the surface layers to an unknown degree. Experiments that base structure determination on an insufficient range of LEED intensity data can also result in inaccurate multilayer relaxations.

In all probability, the Feibelman issue is an accumulation of all the aforementioned experimental and theoretical problems rather than being a product of any single flaw. Previous research by G. Teeter^[1] and D. Hinson^[2] support this postulate by quantifying the affect certain factors (surface roughness, presence of hydrogen) associated with experimental methodology have on multilayer surface relaxations.

IV.3 Review of Previous Work

The primary goal of the previous surface structure research (by Teeter) was to obtain new multi-layer relaxation measurements for transition metal surfaces known

to exhibit large experiment-theory discrepancies, namely Rh(100), W(110), and Ti(0001) with special attention to surface perfection and proper application of LEED methodology. Table III shows a summary of the final results of these relaxation experiments.

A secondary goal of the previous experiments was to examine experimental LEED IV methodology in order to eliminate systematic error as a possible source of the Feibelman issue. The specific issues that were studied are the following: the effect of surface hydrogen contamination, the effect of surface roughness, the reproducibility of independent LEED data sets, the compatibility of independent LEED intensity analysis programs, and the overall energy range of data sets.

The effect of surface hydrogen contamination on multilayer relaxation experiments was tested through EELS studies of residual hydrogen gas on Rh(100), W(110), and Ti(0001). The studies concluded that hydrogen overlayers form too slowly on Rhodium and Tungsten to be a source of error. Titanium is different than rhodium or tungsten because it is highly reactive to hydrogen. As a result of this reactivity, residual surface hydrogen contamination remaining after cleaning is a cause of the measured reduced first-layer relaxation of Titanium. Allowance for surface hydrogen on titanium resulted in a 1st layer relaxation that is closer to ab-initio calculations than other published experimental results.

The effect of surface roughness was tested by comparing LEED structural results obtained from flat and vicinal W(110) surfaces. The results indicate that surface roughness causes insignificant errors to structural calculations, assuming the

surface is ordered well enough to produce a clear diffraction pattern with no apparent splitting from alignment error.

The compatibility of different LEED sets was tested by obtaining surface structure relaxations from two different Rh(001) crystals during separate experiments. The experimental results from both crystals were found to produce similar LEED IV data, but the determined surface structures were incompatible with one crystal producing a (small) first layer contraction and the second crystal producing a (small) expansion. R-factor analysis using several published experimental LEED results^[86,87] corroborated both surface structures, which at the time suggested both structural results could have been correct. It is postulated that one of the Rhodium crystals became strained during in-situ cleaning resulting in the first layer expansion. Other published relaxations that confirm this particular experimental surface structure could also possess slight crystal imperfections (strain, local melting, etc.). Improper in-situ crystal preparation can lead to inconsistent experimental results and contribute to the Feibelman issue. At this time, Rh(001) is known to exhibit a small relaxation in agreement with theoretical predictions.

The Feibelman issue might be caused by error within the various computer codes used to analyze intensity data. This issue was test by using the Xerox LEED and the SATLEED program to calculate structural relaxations for Rh(001). The structural results of both programs were compatible, eliminating systematic errors in intensity analysis codes as a possible source of error.

The energy range of the experimental measurements is known to affect structural results, but its significance to the Feibelman issue is not known. This was tested by graphing the convergence of structural parameters versus the energy range of the experimental IV curve data for W(110). The conclusion from this test is that part of the experiment-theory relaxation discrepancy could result from insufficient experimental energy range of data sets and that a minimum overall energy range of 1000 eV is needed to obtain meaningful structural results.

Rh(001) Experiment	$\Delta d_{12}/d_0(\%)$	$\Delta d_{23}/d_0(\%)$
<i>Begley et al.</i>	-1.4 ± 3.6	
Teeter	-1.4 ± 1.4	-0.6 ± 1.4
Rh(001) Theory	$\Delta d_{12}/d_0$	$\Delta d_{23}/d_0$
<i>Cho and Scheffler (GGA)</i>	-1.4	
(LDA)	-3.0	-0.2
W(110) Experiment	$\Delta d_{12}/d_0$	$\Delta d_{23}/d_0$
<i>Arnold et al.</i>	-3.1 ± 0.6	0.0 ± 0.9
Teeter	-3.0 ± 1.3	0.2 ± 1.3
W(110) Theory	$\Delta d_{12}/d_0$	$\Delta d_{23}/d_0$
<i>Arnold et al.</i>	-3.6	+0.2
Ti(0001) Experiment	$\Delta d_{12}/d_0$	$\Delta d_{23}/d_0$
<i>Shih et al.</i>	2.0 ± 2.0	
Teeter	-4.9 ± 1.0	1.4 ± 1.0
Ti(0001) Theory	$\Delta d_{12}/d_0$	$\Delta d_{23}/d_0$
<i>Feibelman et al.</i>	-7.8	

Table III. Summary of selected previous relaxation experiments. Known experimental and theoretical relaxation values are listed for comparison. The Feibelman issue is resolved for W(110) and Rh(001) but only improved upon for Ti(0001) where the presence and effects of H remain an issue.

IV.4 Hydrogen Uptake Kinetics in Niobium

Many hydrogen adsorption experiments have concentrated on Niobium due to its high sticking coefficient for chemisorption yet low bulk hydrogen uptake rate at

room temperature. The discrepancy between theoretical and experimental multilayer relaxations in niobium may be associated with the unusual hydrogen uptake kinetics operating near the surface. Several theoretical models have been postulated to explain the absorption kinetics of hydrogen in Nb(100), such as the surface-hydride and sub-surface valve models, but no model has been systematically tested experimentally.

Early experiments by M.A. Pick^[23] attempting to understand the adsorption of hydrogen gas on niobium surfaces focused on niobium's ability to absorb large amounts of hydrogen when the surface is covered by a monolayer of Pd. Greater concentrations of hydrogen atoms diffused into the bulk of palladium-covered niobium than for the clean-surface Niobium crystal. It is believed the palladium decreases the depth of the potential well(s) in the surface region allowing a higher diffusion rate for adsorbed hydrogen.

The results of these experiments led Pick to postulate the dilute phase model (DPM) of hydrogen diffusion. The dilute phase model asserts that a dilute hydrogen phase exists on the niobium surface in equilibrium with the concentration of bulk hydrogen. The concentration of hydrogen at the surface or in the bulk depends on the temperature of the crystal and the difference between the heats of solution and desorption. The bulk solution energy of niobium is much less than the bulk desorption energy; this results in a higher concentration of hydrogen on the surface than in the bulk. The model also predicts that the rates of hydrogen absorption into

the bulk and hydrogen adsorption on the surface decrease simultaneously over time, illustrated in figure 7.

Angle-resolved photoemission spectroscopy on Nb(110) by R.J. Smith^[24] was the first experiment to test the dilute phase model. Smith explored the H-Nb interaction at Nb(110) by determining the location of the hydrogen atoms relative to the surface atomic layers. The experiment measured the rate of hydrogen transfer between the niobium bulk and surface, and then analyzed the results using the dilute phase model. The conclusions of this experiment were the following: the time dependence of hydrogen saturation at the surface does not follow DPM predictions at any temperature, the time dependence of surface hydrogen coverage indicates high sticking rates with no equilibrium between surface and bulk concentrations of hydrogen, the saturation value of the surface coverage at room temperature coexists with a much smaller bulk concentration than is indicated by the DPM implying a decoupled surface and bulk below 300K.

The surface-hydride model attempts to correct the deficiencies of the dilute phase model by substituting an ordered “hydride” phase as a replacement for the dilute hydrogen phase that will rapidly precipitate on the niobium surface for high hydrogen concentrations and low temperatures. After a hydride layer forms on the surface, strong H-H interactions change the surface kinetics to achieve equilibrium between the hydride surface layers and the bulk. The hydride clusters\layers^[25] on the metal surface limit the diffusion of hydrogen into the niobium bulk leading to a linear bulk diffusion rate. The model also claims that at low hydrogen concentrations and

high temperatures all surface hydrogen atoms diffuse directly into the bulk as stipulated by the DPM. The desorption of bulk hydrogen or absorption of surface hydride clusters into the bulk is a reversible process as sample temperature is decreased or increased. Figure 7 illustrates the saturation curves for surface (θ) and bulk (x) concentrations of hydrogen (N_H) according to the dilute phase and surface-hydride models at low temperatures.

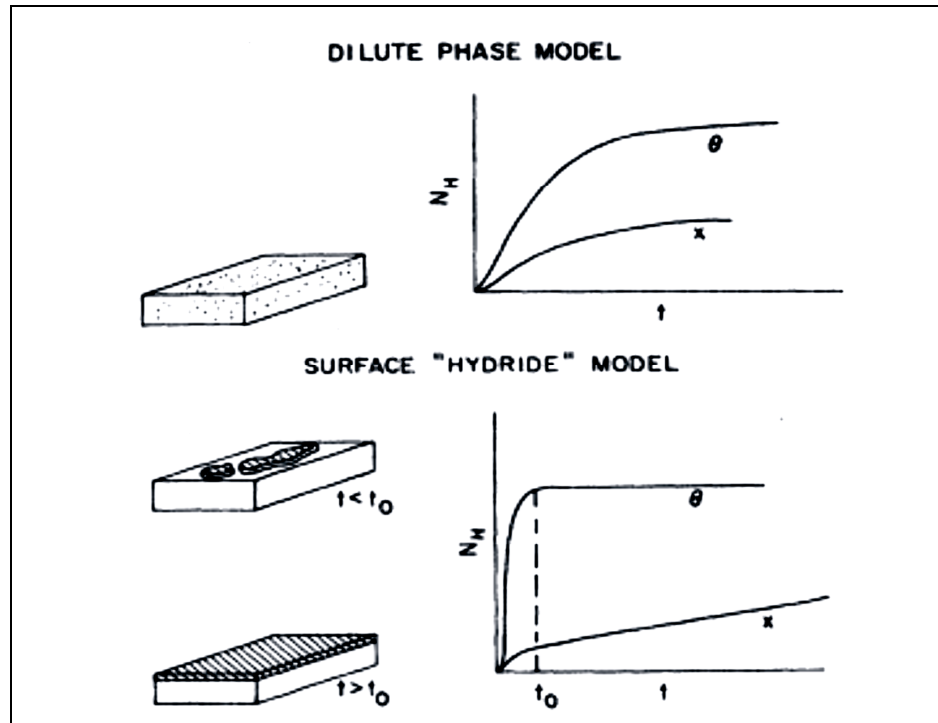


Figure 7. The time when the hydride clusters cover the surface is marked as t_0 . Surface hydrogen adsorption is rapid and then reduces to zero at complete coverage with bulk diffusion becoming linear.

The sub-surface valve model attempts to correct the deficiencies of the dilute phase model with the addition of a near-surface hydrogen state. The sub-surface valve model claims that a deep sub-surface potential well exists between the

chemisorption site well at the surface and the well associated with hydrogen in Niobium bulk lattice sites. The hydrogen binding energy of the chemisorption site well (the first sub-surface bonded state) is much weaker than the binding energy of the deep sub-surface potential well (the second sub-surface bonded state)^[26,27]. Sub-surface trapping is significant and it is energetically favorable to completely fill the second sub-surface bonded state before any diffusion occurs^[28]. Strong inter-atomic bonding between the trapped sub-surface hydrogen atoms blocks any diffusion of surface hydrogen into the bulk making further absorption difficult.

The sub-surface hydrogen layers become a temperature-dependent valve that allows reversible hydrogen diffusion between the surface and bulk. The temperature-dependent valve relies on a critical temperature to determine the rate of hydrogen diffusion. At temperatures below the critical temperature sub-surface hydrogen is trapped by the potential well and the surface valve is closed resulting in high hydrogen concentrations in the “surface” region. The surface and bulk hydrogen concentrations are completely decoupled at these temperatures. At temperatures above the critical temperature, trapped hydrogen atoms are energetic enough to overcome the sub-surface potential well permitting diffusion at a rate close to DPM predictions. As a consequence, the diffusion of large quantities of hydrogen creates equilibrium between the surface and bulk hydrogen concentrations. Figure 8 illustrates how the rate of hydrogen diffusion is a function of the sample temperature.

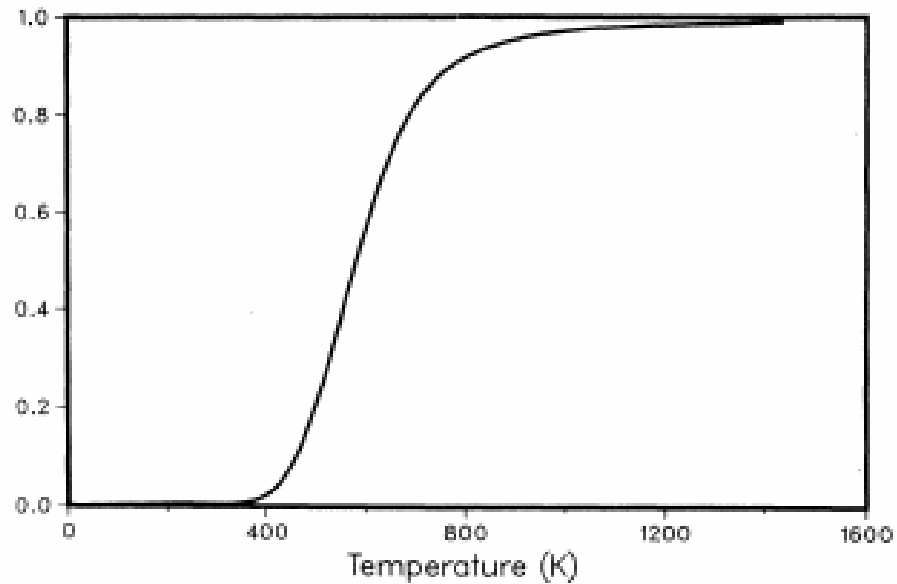


Figure 8. The temperature dependence of the “surface valve” rate of hydrogen diffusion is shown as a function of temperature vs. valve “openness”, assuming a critical temperature (T_c) of 600K.

Angle-resolved photoemission experiments have proven that there are at least two states which have hydrogen bonded to the Nb(100) surface, with one or both existing in the sub-surface region^[30-31,53]. Photoemission experiments and inelastic electron scattering experiments confirmed the sequential exchange of hydrogen atoms between two sub-surface bonded states in Niobium at low temperatures, and the depletion of surface and sub-surface hydrogen to the bulk at high temperatures^[26]. Both photoemission experiments conclude that the sub-surface valve model for hydrogen diffusion is a better explanation of experimental results than the surface-hydride model, but there have been no definitive surface structure experiments (i.e. LEED study of the H/Nb(100) surface) that have addressed this issue. This is one objective of the present research.

IV.5 Surface Magnetism in V(100)

Surface magnetism in vanadium has been a research subject since the late 1970's when Akoh and Tasaki^[32] conducted experimental studies that found large localized magnetic moments in small vanadium particles. The magnetic moments were believed to originate in the surface region of vanadium, even though the bulk metal is known to be paramagnetic. Subsequent ab-initio calculations attempted to explore the magnetic polarization of a vanadium surface, but these calculations produced conflicting results^[33-40]. The surface of vanadium varied from ferromagnetic to paramagnetic depending on the type of ab-initio approach (pseudopotential, FLAPW, surface Coulomb exchange integral, etc.) that was employed.

The only experimental evidence supporting two-dimensional magnetism in a vanadium surface is an electron-capture spectroscopy experiment by C. Rau^[41]. The electron-capture spectroscopy experiment^[41] reported in 1986, detected strong spin polarization of V(100) at 300K that vanished at the Curie temperature (540K). Magnetizing fields along the [001] direction ranging in strength from 103 to 515 Oe were found sufficient to maintain magnetic saturation (no change in detected spin polarization). Surface oxygen contamination of 0.06 monolayer (6%) at 300K was found to reduce the spin polarization from 30% to 22%. These experimental results were interpreted as evidence of first-layer long-range ferromagnetic ordering of

V(100) with anisotropy energy low enough to be overcome at 300K by an in-plane applied field of 103 Oe, and a Curie temperature $T_c = 540\text{K}$.

This magnetic moment result is widely cited in publications dealing with surface magnetism, especially ab-initio calculations for V(100)^[36,38] surfaces, but has been viewed with skepticism because another Rau electron-capture spectroscopy experiment also detected ferromagnetic order in the top layer of p(1 x 1) V on Ag(100)^[42], whereas magneto-optic Kerr effect studies^[43] failed to detect ferromagnetism, and a subsequent ab-initio calculation^[44] reported that p(1 x 1) V on Ag(100) is paramagnetic.

The Rau experiments^[41,42] report of ferromagnetic order at the surface of vanadium have helped sustain interest in resolving the significant differences^[39] in the magnetic properties of V(100) predicted by two principle classes of theoretical approaches: pseudopotential calculations vs. all-electron calculations. Table IV summarizes some of the recent values of surface magnetic moments for V(100) predicted based on various ab-initio approaches. The general trend that emerges from Table IV is the prediction of ferromagnetic ordering at the surface by pseudopotential methods and the absence of magnetism predicted by the all-electron methods^[34-39]. This issue has been reviewed in relation to results for V(100) by Robles et al^[39], and Batyrev et al^[36].

Table IV

Calculation	$\mu_B(\text{Surface})$
Bihlmayer et al ^[37]	
(7 Layer)	0.04
(15 Layer)	0.00
Batyrev et al ^[36]	0.75
Robles et al ^[39]	
GGA\LMH	0.66
GGA\PW	0.25
LSDA(AE\PP)	--
Experiment	e ⁻ spin Polarization
Rau ^[41]	-34%
(0.06 ML Oxygen)	-20%

Table IV. Magnetic moment in Bohr magnetons corresponds to first-layer spin polarization. The lattice constants used during these calculations are listed in Table VIII.

Experimental issues that could affect magnetism studies in V(100) are surface hydrogen impurities, large surface-layer relaxations, and the feasibility of unambiguous detection of single-layer ferromagnetism. Techniques that measure magnetism using multiple atomic surface layers such as the magneto-optic Kerr effect

and spin-polarized photoemission, might not detect single-layer surface ferromagnetism due to the paramagnetism of other near-surface layers. The primary experimental issue relating to surface ferromagnetism in V(100) is the validity of the Rau electron-capture spectroscopy experiment^[41], one objective of this research is to confirm or refute this result.

V. Temperature-Dependent Multilayer Relaxation of Clean and Hydrogen-Dosed Nb(100)

V.1 Introduction

The surface electronic structure of Nb(100) has been investigated by photoemission^[24,26,30-31,50-52], the vibrational properties have been investigated by inelastic electron^[53] and He atom^[54] scattering, but the only attempt at a surface structure determination appears to be a study of photoelectron diffraction^[55]. There are numerous ab-initio calculations that explore the electronic, vibrational, and structural properties of bulk Nb^[56], Nb hydrides^[57], and Nb surfaces^[58-61], but there appear to be no prior measurements of closely-related multilayer surface relaxation of any Nb surface by low-energy-electron diffraction (LEED).

This chapter presents a LEED investigation of multilayer relaxation of Nb(100) including the effects of hydrogen. The results are relevant to recent ab-initio calculations of surface properties of reactive transition metal surfaces, and various prior studies of hydrogen uptake kinetics and chemisorption of hydrogen at Nb(100). These prior studies suggest that the properties associated with the hydrogen-Nb(100) surface are governed by hydrogen atoms at tetrahedral lattice sites near the surface. The results presented in this chapter also extend our study^[6-8,62] of trends in multilayer relaxation of reactive transition metal surfaces. This experimental

program was stimulated by systematic inconsistencies^[3,4] between top-layer relaxation obtained from ab-initio calculations and corresponding results from LEED crystallography described in Chapter IV and by Table I.

V.2 Sample Preparation

In-situ cleaning, surface characterization, and structure measurements were carried out using a UHV instrument that incorporates LEED, Auger electron spectroscopy (AES), electron-energy-loss spectroscopy (EELS), and ultraviolet photoemission (UPS) capabilities. The LEED intensity-versus-voltage (I-V) spectra were measured using frame-grabbing instrumentation interfaced to a SIT camera described in Chapter II. The instrument base pressure with liquid-nitrogen cooled Ti sublimation pumping ($< 5 \times 10^{-11}$ Torr) is adequately low to reduce undesired H and CO surface contamination during the (40min) periods required to log a set of I-V spectra to below 0.01 – 0.02 monolayer (ML).

Clean surface preparation of Nb(100) presents significant challenges. Nb is a 4d metal that lies just below V (3d metal) in the Periodic Table. Both V and Nb exhibit high reactivity to and solubility of hydrogen and other elements, including carbon and oxygen. Furthermore, additional carbon and oxygen contamination is always present on a surface after a long high-sensitivity AES scan (30 min.) or after logging LEED spectra (40 min.) due to CO production from the tungsten filaments. The best efforts to date have yielded only technically-clean surfaces of both Nb(100) and V(100). In the case of V(100), bulk carbon limits the cleanliness of a prepared surface to 4-5% carbon^[33,62]; for Nb(100) the strong chemical affinity, high solubility,

and high desorption temperature associated with oxygen and the Nb surface have limited the purity of technically-clean Nb(100) to about 8% oxygen. Fortunately, recent detailed characterization of ordered surface chemisorbed layers (oxygen for Nb(100)^[63] and carbon for V(100)^[33, 64]) based on AES and scanning tunneling microscopy (STM) have established accurate adsorbate coverages referenced to AES peak ratios, and these surface coverage calibrations permit extrapolation of LEED measurements of the multilayer relaxation of technically-clean surfaces to clean surface values^[62].

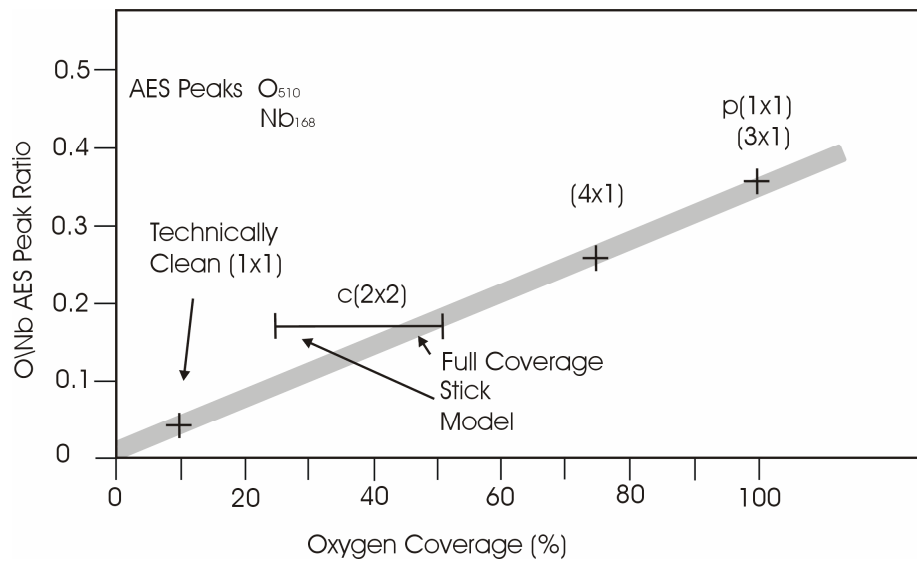


Figure 9. $\text{Nb}_{168}/\text{O}_{510}$ Auger electron spectroscopy peak ratios for calibrated oxygen coverages on Nb(100) based on scanning tunneling microscopy experiments of An et al (ref. 63). The (3 x 1) Nb(100) reconstruction occurs at saturation oxygen coverage. The point labeled “technically clean” corresponding to an AES peak ratio of 0.4 represents the lower limit of the surface oxygen concentration achieved in the experiments (8-10%).

Figure 9 summarizes AES peak ratios ($\text{O}_{510}/\text{Nb}_{168}$) for ordered oxygen overlayer models based on STM studies of oxygen-dosed Nb(100)^[63]. The plotted

coverage is based on the fraction of four-fold Nb(100) sites filled by oxygen atoms. The STM images reveal islands and some top-layer Nb atom reconstruction that reduce the effective coverage compared to an ideal coverage model. In the case of the c(2 x 2) structure, a “stick” structure reduces the coverage from the ideal value ($\Theta = 1/2$) to $\Theta = 1/4$. This “stick” reconstruction behavior brings the c(2 x 2) oxygen AES peak ratio into reasonable agreement with the coverage-dependent ratios established for the other ordered layers. The lowest O_{510}/Nb_{168} peak ratio achieved in our extensive efforts to clean Nb(100) was $O_{510}/Nb_{168} \lesssim 0.04$ which according to the calibration data (Fig. 9) corresponds to an oxygen contamination level of about 8%.

Because of the relatively high mobility of oxygen in Nb, it is possible to attribute some uncertainty to the calibration of surface oxygen contamination in terms of the AES O/Nb peak ratio based on STM images, because STM is not sensitive to subsurface oxygen. However, there is no evidence^[53] that the oxygen present at a technically-clean Nb(100) surface is below the surface (as is clearly the case for hydrogen), therefore, the oxygen AES calibration result obtained from Fig. 9 is believed to be accurate.

The Nb(100) sample used in experiments described in this chapter was cut from an oriented single-crystal boule (99.9+% purity). The 12mm dia x 2mm thick sample was spark cut by an electric discharge milling machine using a moving wire electrode. The sample was aligned using x-ray Laue back-diffraction techniques assisted by Orient Express software^[11]. After mechanical polishing using alumina

and diamond abrasives to 0.25 μm particle size, the (100) crystal axis was determined to be aligned with the surface normal to an accuracy exceeding $\pm 0.5^\circ$. The surface-step density and roughness associated with this orientation accuracy is below the detection limit of conventional LEED optics (for observing spot splitting) and far below the step density threshold shown to result in structure determination errors based on LEED intensity measurements^[55].

The sample was mounted on a manipulator at the tip of a UHV liquid nitrogen dewar that permitted precise orthogonal two-axis rotation about the crystal face. This orientation capability was used to align the (100) crystallographic axis parallel with the incident electron beam from the LEED optics. The sample could be heated by an electron beam from the back and could be cooled to 150K. A Chromel-Alumel thermocouple attached to the crystal (in addition to a handheld pyrometer with an infrared filter) was used to measure sample temperature.

Extensive in-situ sample cleaning and annealing was required to achieve a “clean” and well-ordered surface. Sample conditioning consisted of repeated cycles of ion sputtering at glancing incidence (ion gun operating at 15mA emission, 2KV and 1×10^{-4} Torr Ne yielding $\sim 10 \mu\text{A}$ current at the sample) followed by high-temperature annealing. Ion sputtering and annealing to within 200K of the melting temperature (2740K) yielded a technically-clean Nb(100) surface that was free of all impurities (except oxygen) to the sensitivity limit of AES (estimated to be 1%), and an oxygen concentration of about 8%.

V.3 LEED Data and Analysis

LEED intensity vs. voltage (I-V) data sets were acquired after symmetrizing conjugate (symmetry-degenerate) beam intensities as described previously ^[23,65-67]. Typical Pendry (r_p) and Zanazzi-Jona (r_{zj}) r-factors for conjugate beam/averaged beam comparison of unsmoothed I-V spectra for five “clean” Nb(100) data sets are: (10) beams (450 eV range) $r_p \sim 0.163$, $r_{zj} \sim .052$; (11) beams (350 eV range) $r_p \sim 0.152$, $r_{zj} \sim .052$; (20) beams (300 eV range) $r_p \sim 0.124$, $r_{zj} = 0.055$; (21) beams (200eV range) $r_p \sim 0.156$, $r_{zj} \sim 0.041$. Corresponding values for five hydrogen-dosed Nb(100) data sets are: (01) beams, $r_p \sim 0.136$, $r_{zj} \sim 0.028$; (11) beams, $r_p \sim 0.159$, $r_{zj} \sim 0.048$; (20) beams, $r_p \sim 0.146$, $r_{zj} \sim .047$; (21) beams, $r_p \sim 0.145$, $r_{zj} \sim 0.040$. The low r-factors indicate good alignment of the incident beam along the (100) crystal axis.

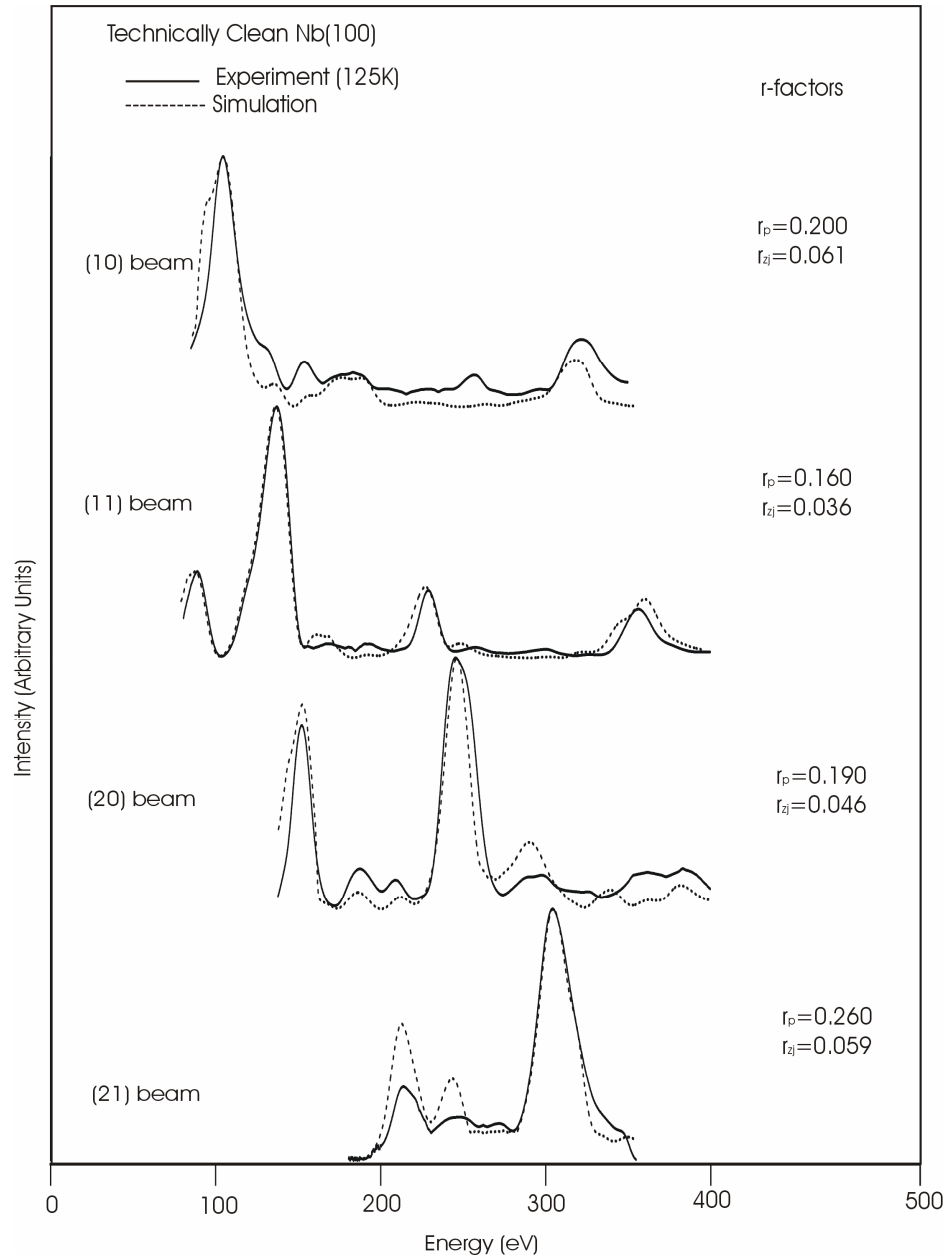


Figure 10. LEED intensity spectra for Nb(100) plotted with corresponding intensity simulations and Pendry (r_p) and Zanazzi-Jona (r_{zj}) r-factors that characterize the fit.

The Barbieri/Van Hove SATLEED code^[13] was used to numerically simulate the measured IV spectra. A typical example of an optimized simulation is shown in

Fig. 10 with the corresponding I-V data set and r-factors that characterize the fit. The calculations are based on 13 relativistic phase shifts, which were also calculated using the Barbieri/Van Hove code. Convergence tests in which r-factors and structure parameters were evaluated as a function of the number of phase shifts used in the analysis revealed no differences for $l_{\max} \geq 6$. Standard r-factor analysis based on r_p and r_{zj} was used to optimize structural and non-structural parameters leading to structure determination based on the I-V spectra. The application of both r_p and r_{zj} criteria yielded essentially the same structural results. All calculations for both technically-clean and hydrogen-dosed Nb(100) were carried out using a surface structural model that allowed multilayer relaxation of the top three layers, but no lateral displacements of the atoms within a plane. This assumption is consistent with STM studies^[63] of Nb(100) and with the $p(1 \times 1)$ LEED patterns observed in our experiments that manifest no evidence of surface reconstruction.

LEED simulations for the hydrogen-dosed Nb(100) surface were carried out using the same multiple scattering model (crystal unit cell) used for the “clean” surfaces. Neglecting the weak scattering from hydrogen atoms is justified, based on prior LEED experiments on clean and hydrogen-dosed Rh(001)^[6]. In that study, two structural models were applied to experimental I-V spectra obtained from a saturated coverage of H on Rh(100). One model neglected scattering from hydrogen atoms, a second model included hydrogen atoms in the (lowest total energy) fourfold hollow sites. Both simulations converged to the same model for the multilayer surface

relaxation (within $\pm 0.01 \text{ \AA}$). Based on multilayer relaxation results for hydrogen-dosed Nb(100), presented later, a LEED I-V analysis was also carried out assuming that the bulk Nb(100) surface was terminated by a single unit cell of bulk βNbH . This model did not provide a better fit to experimental data for hydrogen-dosed Nb(100).

V.4 Clean and Technically Clean Nb(100) Structure

Density-functional-theory calculations provide a means of studying trends in physical parameters associated with metal surfaces such as surface energies, workfunctions, and surface relaxation, as well as chemical phenomena such as chemisorption^[59, 68]. The study of trends for high-index crystallographic surfaces of a series of metals (for example the 4d transition metals) offers important opportunities for testing simple models of surface behavior and for gaining insight into the physical processes that govern the trends. For example, the tendency of sp electrons to spread smoothly at a surface, coupled with the directional forces associated with localized d electrons, has been used to account for various trends observed in the surface relaxations and chemical behavior of transition metal surfaces.

A key element in assessing the validity and accuracy of ab-initio calculations of surface properties has been the comparison of calculated multilayer surface relaxation with corresponding results obtained by electron diffraction experiments. Tests based on other information, such as work functions, occurrence of magnetic ordering or magnetic dead layers, the tendency of certain bcc surfaces (i.e., W(100)

and Mo(100)) to reconstruct, and electronic structure specific to a surface (electronic surface states and resonances) have also been used to test predictive accuracy of ab-initio calculations, but multilayer surface relaxation seems to have become the traditional standard test. This is a logical choice because the position and coordination of surface atoms is a ground state property that governs other physical properties, including surface and thin-film magnetism and surface electronic structure; and the structure can, in principle, be accurately determined (by LEED). The use of electronic binding energies and band widths determined by photoemission as a means of evaluating accuracy of calculations may be a less favorable criteria because these parameters involve excitations that introduce questions about energy shifts resulting from many-body effects.

Although the comparison of calculated and measured multilayer surface relaxations has been adopted as one of the most important tests of the predictive accuracy of ab-initio methodology, significant (and apparently systematic) discrepancies between experimentally and theoretically-determined multilayer relaxations have been noted^[3,4] and described in Chapter II. Ab-initio methods generally reproduce quite accurately bulk lattice parameters obtained by x-ray diffraction; therefore, the corresponding discrepancies for surface structure, which in many cases exceeds the claimed accuracy of both the LEED methodology and the calculations, has caused some concern. Some of the existing discrepancies have been recently accounted for in terms of the effects driven by low concentrations of (undetected) hydrogen^[8] or other surface impurities^[33, 62] that increase the

coordination of surface atoms. Increased coordination of surface atoms tends to reduce top-layer relaxations. These results justify re-evaluation of some of the existing LEED structure determinations with special attention to the level of surface impurities, as well as new LEED experiments using surfaces for which ab-initio calculations have included predictions of multilayer relaxation, i.e. Nb(100).

Calculation	Δ_{12}	Δ_{23}	Δ_{34}
TBA 20 Layer Slab ^[61]	-11.65	--	--
TBA ^[60]	-12.1	+10.7	-5.6
DFT/LDA 7 Layer Slab ^[59]	-9.3	--	--
TBA/MD ^[58]	-6.3	-0.7	--
Experiment			
Photoelectron Diffraction ^[55]	-13.5	--	--
LEED (Extrapolated)	-10.0	+5.5	--
LEED ((1x1) 9% Oxygen)	-7.2	+3.5	-3.1
((2x2) 20% Oxygen)	-5.2	+1.7	-3.6

Table V. Calculated and measured surface relaxations for Nb(100). Interplanar relaxations $\Delta_{ij} = d_{ij}/d_0$ are presented as a percentage of the bulk lattice separation d_0 .

Table V summarizes the available surface structure information for Nb(100) derived from ab-initio calculations, and from the only existing experimental result

(based on photoelectron diffraction) for top-layer relaxation. The results displayed in Table V represent one of the few cases where an existing experimentally-determined top-layer relaxation is greater than typical values obtained from ab-initio calculations. Also summarized in Table V are our LEED results for Δ_{ij} for extrapolated clean, and technically clean ($\sim 8\%$ oxygen) surfaces. Hydrogen dosed experiments are described in the following section.

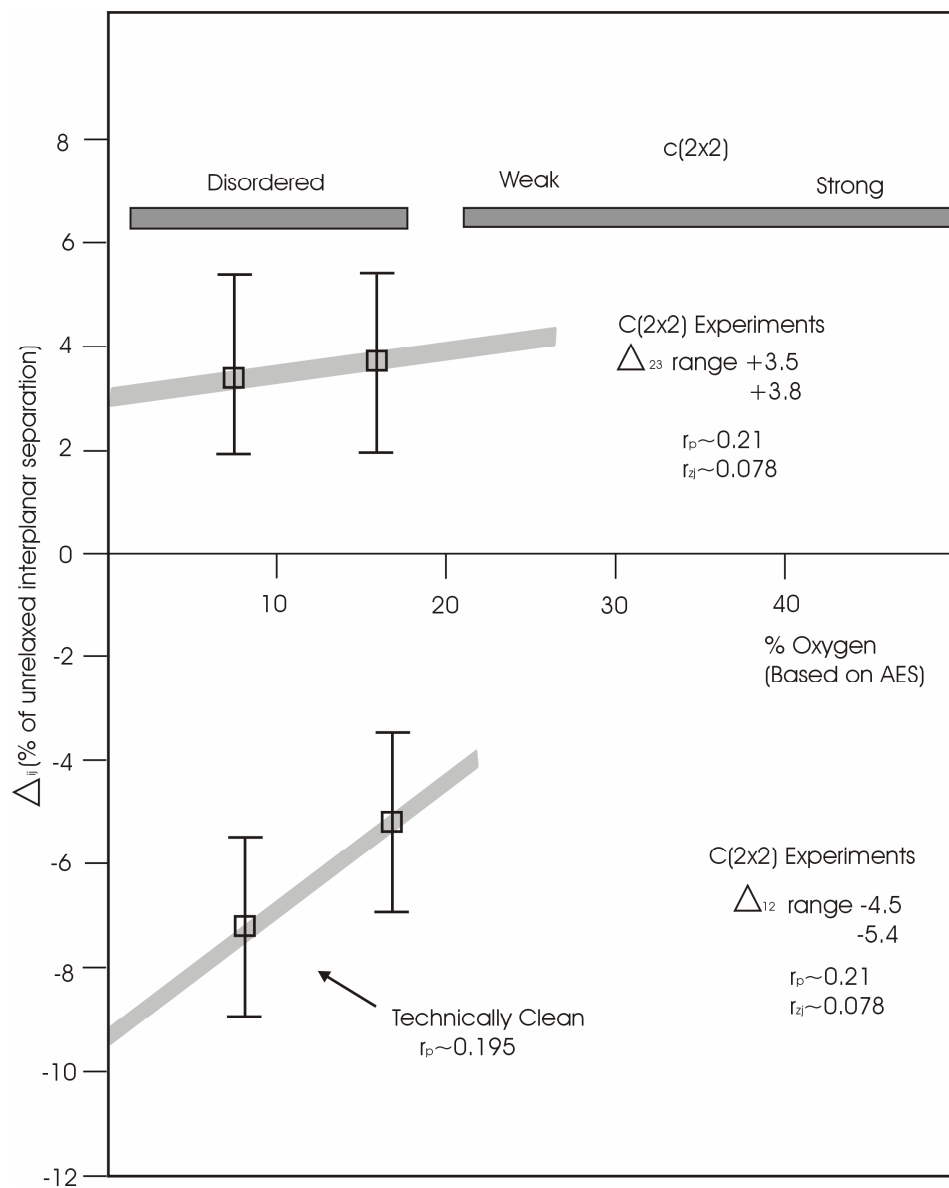


Figure 11. Graphical illustration of the range of ordered c(2 x 2) and disordered chemisorbed oxygen on Nb(100) with LEED values for first (Δ_{12}) and second (Δ_{23}) layer relaxations at two oxygen concentrations. The extrapolated value of Δ_{12} to zero oxygen coverage is $\Delta_{12} \sim -10\%$.

Figure 11 displays values of Δ_{12} and Δ_{23} (first- and second-layer relaxation) for Nb(100) with an ordered c(2 x 2) oxygen surface layer and for technically-clean

p(1 x 1) Nb(100) with an estimated (disordered) oxygen concentration of $\sim 8\%$. The oxygen concentration is based on the AES calibration described in Fig. 9. The r_p values obtained in fits for p(1 x 1) technically-clean Nb and c(2 x 2) oxygen on Nb(100) are low enough to be able to place high confidence in the LEED-determined value of Δ_{ij} . For example, similar values of r_p were obtained in a LEED analysis of clean Rh(100), $r_p \sim 0.30$ for 100K datasets; W(100), $r_p \sim 0.202$ for 400K data sets; technically-clean Ti(0001), $r_p \sim 0.140$ for 125K data sets, and technically-clean V(100) described later, $r_p \sim 0.223$ for 150K data sets. In these experiments, technically-clean surfaces corresponded to 20% hydrogen for Ti(0001) and 6% carbon for V(100). Our extrapolated clean surface value of Δ_{12} is in good agreement with the result obtained from the most recent ab-initio calculation.

	T(K)	$\Delta d_{12}(\%)$	$\Delta d_{23}(\%)$	$\Delta d_{34}(\%)$	r_p	r_{zj}
Clean	125K	-7.2	+3.5	-3.1	0.196	0.049
	125K	-7.7	+3.6	-3.3	0.160	0.035
	300K	-6.9	+3.6	-4.2	0.213	0.039
	300K	-6.4	+3.3	-4.2	0.217	0.046
	400K	-6.5	-1.4	-5.7	0.188	0.052
Hydrogen	125K	-4.5	+5.7	-5.4	0.201	0.074
	125K	-4.7	+5.7	-3.6	0.199	0.065
	300K	-5.0	+4.5	-8.0	0.250	0.083
	300K	-5.5	+2.7	-8.0	0.195	0.055
	400K	-6.0	+3.6	-3.0	0.163	0.069

Table VI. Multilayer relaxation determined by LEED for technically-clean Nb(100) and (1L) hydrogen-dosed Nb(100) at three temperatures. Pendry (r_p) and Zanazzi-Jona (r_{zj}) r-factors associated with experiment/simulation are displayed for each structure determination.

V.5 Hydrogen Dosed Nb(100)

Table VI presents a more detailed account of experimental results for Δ_{ij} obtained from LEED analysis of technically-clean and hydrogen-dosed Nb(100). Several datasets were obtained at three temperatures. The minor differences in Δ_{ij} at different temperatures is attributed to the ability of Nb to absorb hydrogen into the bulk, especially at elevated temperature, and the fact that the best technically-clean Nb(100) surfaces exhibited easily-detected (by AES) oxygen contamination ($\sim 8\%$). The hydrogen contamination of the technically-clean Nb(100) was judged low ($<1\%$) based on the base pressure ($\sim 5 \times 10^{-11}$ torr) and previous experience with evaluating the effects of hydrogen contamination at similar base pressure^[8,62].

The hydrogen-dosed surface structural data exhibit temperature-dependent trends in multilayer relaxation that are consistent with prior photoemission^[24,26,30-31,50-52], inelastic electron scattering^[53], and adsorption/desorption kinetics^[28,47-49] experiments that probe the hydrogen-Nb(100) surface system. These experiments probed temperature-dependent electronic (photoemission) and vibrational (inelastic electron scattering) properties associated with hydrogen-dosed Nb(100) that were interpreted to result from the effects of hydrogen in tetrahedral subsurface sites. Both experiments exhibited reversible temperature-dependent effects produced by hydrogen dosing that provided indirect experimental evidence of the self-trapped subsurface valve model. Our new LEED results for multilayer surface relaxation of

hydrogen-dosed Nb(100) provide more direct evidence for the subsurface hydrogen sites and additional support for the model of uptake kinetics based on these sites.

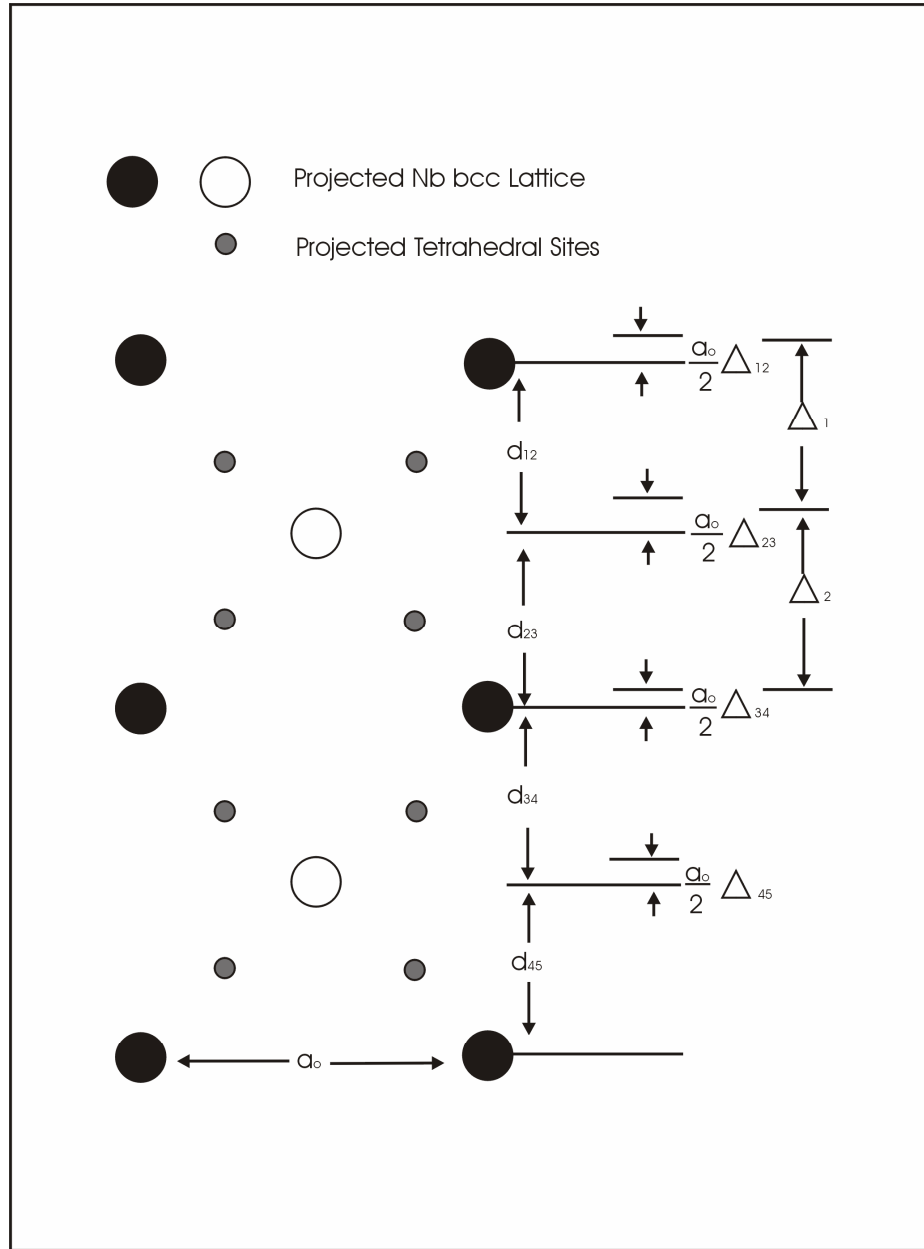


Figure 12. Side view of Nb(100) lattice showing projected location of hydrogen (tetrahedral sites) and defining the parameters a_0 lattice constant, d_{ij} interplanar separation, Δ_{ij} relaxation parameter, and Δ_i interplanar expansion parameter.

Figure 12 displays a side-view model of the (bcc) Nb(100) surface with symbols that describe various lattice plane displacements and separations. Table VII defines the parameter Δ_i and lists (normalized) values of Δ_1 and Δ_2 obtained from temperature-dependent multilayer relaxation of clean and hydrogen-treated Nb(100). Entries of Table VII that are noted by * highlight values of Δ_2 that manifest significant changes resulting from hydrogen dosing or changes in temperature. The significant changes in Δ_2 resulting from hydrogen dosing result primarily from the large changes of Δ_{34} (Table VI) that occur after hydrogen dosing of Nb(100) below 400K. Note that Δ_2 characterizes the separation of crystallographic planes just below the surface. The change in Δ_2 resulting from hydrogen dosing below 400K corresponds to a unit-cell distortion along the (100) direction of 3-4%. Formation of bulk NbH results in a change in the (bcc) lattice constant from $a_0 = 3.29\text{\AA}$ to $a_0 = 3.44\text{\AA}$ (β phase) or $a_0 = 3.46$ (δ phase) corresponding to an expansion of 4.5% (β phase) or 5.2% (δ phase).

			125K	300K	400K
$\Delta_1 = \frac{a_o}{2} (1 + \Delta_{12} - \Delta_{23})$	$\frac{2\Delta_1}{a_o}$	Clean	0.89	0.89	0.90
		Hydrogen	0.90	0.91	0.90
$\Delta_2 = \frac{a_o}{2} (1 + \Delta_{23} - \Delta_{34})$	$\frac{2\Delta_2}{a_o}$	Clean	1.07	1.08	1.07
		Hydrogen	1.10*	1.12*	1.06
Bulk Nb		$a_o = 3.29$			
δ NbH		$a_o = 3.46$ (5.2% Expansion)			
β NbH		$a_o = 3.44$ (4.5% Expansion)			

Table VII. Temperature-dependent near-surface lattice expansion ($2\Delta/a_o > 1$) or contraction ($2\Delta/a_o < 1$) relative to bulk Nb value $a_o/2$ for clean and hydrogen-dosed Nb(100). Note that normalized values of Δ_i ($2\Delta_i/a_o$) are shown in the table. Table entries highlighted by * exhibit significant temperature-dependent and hydrogen-dose dependent changes

The observed changes in multilayer surface relaxation of technically-clean Nb(100) as a function of temperature for a hydrogen-dosed surface are consistent with prior experiments that explore subsurface hydrogen at Nb(100). The results manifest strong evidence of lattice expansion for $T < 400\text{K}$ attributed to hydrogen atoms occupying tetrahedral sites in the lattice near the surface. The measured expansion of the near surface lattice (Δ_2 = separation between second and third lattice planes) is $3 \pm 1\%$ at 125K, $4 \pm 1\%$ at 300K, and $-1 \pm 1\%$ at 400K. The expansion at $T < 400\text{K}$ is compatible with the change in lattice constant when Nb is hydrated to βNbH (4.5% increase). The relaxation of the lattice expansion to the clean surface

value for $T > 400\text{K}$ is consistent with thermally-driven depopulation of the near-surface hydrogen sites that has been used to explain temperature-dependent changes in the surface electronic and vibrational properties of hydrogen-dosed Nb(100) which supports the subsurface-valve model of novel hydrogen uptake kinetics associated with Nb(100).

V.6 Conclusions

The surface structure of Nb(100) has been investigated by LEED crystallography as a function of temperature and as a function of oxygen coverage and hydrogen dose. The multilayer relaxation of $c(2 \times 2)$ O on Nb(100) and technically clean $p(1 \times 1)$ surfaces with $\sim 8\%$ oxygen contamination were determined by LEED and used to extrapolate the value of top-layer relaxation to a clean surface value $d_{12} = 1.481 \pm 0.05\text{\AA}$ corresponding to a contraction of $-10.0 \pm 3\%$. The value is in reasonably good agreement with recent ab-initio calculations that predict a first-layer contraction at Nb(100) of 10-12% (Table V). The only other available experimental result for d_{12} at Nb(100) is based on photoelectron diffraction $d_{12} = 13 \pm 5\%$ (Table V). Thus the two experiments are compatible based on the error estimates. The photoelectron diffraction result is not accompanied by a meaningful quantitative assessment of the surface oxygen or hydrogen concentration; therefore, any additional comparison or discussion of the two experimental values is unjustified.

Surface vibrational modes for hydrogen-dosed Nb(100)^[53] are consistent with hydrogen atoms at subsurface tetrahedral sites of the Nb lattice (β phase of NbH).

Both vibrational spectroscopy^[53] and photoemission spectroscopy^[26] experiments indicate the existence of a reversible phase transition associated with subsurface site occupancy by hydrogen at Nb(100) that occurs in the temperature range $300 \leq T \leq 600\text{K}$. The hydrogen-induced variation of Δ_2 determined by LEED and displayed in Table VII is consistent with the previously-observed reversible phase transition involving subsurface hydrogen sites at Nb(100), and provides direct structural evidence for the subsurface-valve model based on measured expansion of the near-surface lattice.

VI Multilayer Relaxation and Search for Ferromagnetic Order at the (100) Surface of Bulk Paramagnetic Vanadium

VI.1 Introduction

In this chapter Low-Energy-Electron-Diffraction (LEED) intensity measurements and multiple-scattering analysis for V(100) are presented, supported by an accurate characterization of surface impurity concentrations based on Auger-electron spectroscopy. Vanadium is a high susceptibility paramagnet that can exhibit ferromagnetic behavior under certain conditions^[69-73]. This feature, along with the close relationship between the occurrence of ferromagnetism, atomic coordination, and the relevant surface or bulk lattice parameter, have resulted in extensive use of the V(100) surface as a venue for testing the predictive accuracy of ab-initio calculations^[33,34-40]. Table VIII summarizes some of the recent experimental values of surface magnetic moments and multilayer relaxation for V(100) as well as calculated values based on various ab-initio approaches.

Table VIII

Experiments	$\Delta_{12}(\%)$	$\Delta_{23}(\%)$	$\mu_B(\text{Surface})$
Jensen et al ^[74]	-6.9	+1.0	--
Bergermayer et al ^[33]	-8.6	+1.3	--
Calculations			
Bihlmayer et al ^[37]			
(7 Layer)	-10.4	--	0.04
(15 Layer)	-11.1	+0.7	0.00
Batyrev et al ^[36]	-12.5	+0.9	0.75
Bergermayer et al ^[33]			
VASP\US	-15.7	+0.47	--
VASP\PAW	-13.3	+0.67	--
FLEUR	-11.1	+0.67	--
Robles et al ^[39]			
GGA\LMH	Experimental		0.66
GGA\PW	Lattice		0.25
LSDA(AE\PP)	Constant		--

Table VIII. Recent values of calculated and measured first-layer (Δ_{12}) and second-layer (Δ_{23}) relaxations of V(100). Δ_{ij} are presented in terms of percent change of bulk lattice spacing $d = 1.515\text{\AA}$. Magnetic moment (right column) in Bohr magnetons corresponds to first-layer spin polarization. The experimental lattice constant was used in the calculations of surface magnetization by Robles et al^[78].

Two general trends emerge from Table VIII. One trend is the conflicting prediction of ferromagnetic ordering at the surface by different theoretical calculation techniques^[34-39] (Section IV.4). The second trend apparent from Table VIII is the

tendency of all ab-initio calculations to predict first-layer relaxations (Δ_{12}) of V(100) that are significantly larger than the experimental values^[33, 74] determined by low-energy-electron diffraction (LEED) crystallography. This trend is not unique to V(100).

Efforts to identify a universal basis for the systematic discrepancy between calculated and measured surface relaxations have had limited success. In the specific case of V(100), significant differences in calculated values of Δ_{12} (Table VIII) have been attributed to details of the computational method^[33] applied to surfaces, but the same methods yield essentially identical values for the bulk lattice constants of V ($d_{th}=2.99\text{\AA}$) when the same GGA approximation is utilized to describe the exchange-correlation potential. The theoretically-predicted value d_{th} is in good agreement with the experimental value $d_o=3.03\text{\AA}$ for bulk V.

The cornerstone for understanding the electronic, chemical, and magnetic behavior of surfaces is an accurate atomic structure model of the surface. If ab-initio calculations based on the local density approximation (LDA) are incapable of accurately predicting the equilibrium positions of surface atoms (a ground-state property that can presumably be determined experimentally), one might justifiably question the predictive accuracy of ab-initio calculations when applied to other surface phenomena such as the occurrence of surface magnetism.

One possible source of structure-determination inaccuracy has been identified in surface crystallography experiments. This inaccuracy is related to the effects of

surface hydrogen. The problem arises because the predominate residual gas in ultrahigh vacuum systems (base pressure in the 10^{-11} Torr range) is H_2 . Hydrogen dissociatively adsorbs on transition metal surfaces, and atomic hydrogen cannot be detected by Auger electron spectroscopy (AES), the most common probe of surface cleanliness. Low concentrations (below 10%) of disordered impurities on an otherwise well-ordered single crystal metal surface results in lower reliability factors (r-factors) in LEED analysis and smaller values of the actual as well as the determined top-layer relaxation. The difference between the clean surface relaxation determined by LEED analysis, and the corresponding result from a slightly contaminated surface (concentration $<10\%$), scales linearly with impurity concentration similar to other parameters, such as the workfunction, that are strongly influenced by charge-transfer effects associated with surface chemical bonding^[68]. A significant reduction of the clean-surface relaxation resulting from undetected surface hydrogen or other impurities at concentrations below the AES sensitivity limit could account for some of the disagreements between calculated and measured structural parameters as outlined in the previous chapter for Nb(100).

This chapter describes experiments that address the surface structure and magnetism of V(100) from the viewpoint of issues outlined in the introduction. The experiments strive to answer two key questions that are relevant to predictions based on ab-initio calculations for V(100): 1) what is the first-layer relaxation, and 2) is the surface magnetic. Because it has not been possible to prepare a perfectly clean and perfectly ordered V(100) surface, these two questions (and answers) must be

modified to reflect experimental limitations. However, the results presented still provide a meaningful basis for judging the predictive capabilities of various forms of ab-initio calculations that have been extensively applied to V(100).

VI.2 Experimental Procedures

The surface structure measurements were carried out using a UHV instrument that incorporates LEED, Auger electron spectroscopy (AES), electron energy loss spectroscopy (EELS), and ultraviolet photoemission spectroscopy (UPS) capabilities. The LEED intensity versus voltage (I-V) spectra were measured by frame-grabbing instrumentation interfaced to an SIT camera. The UHV instrument has been described in the prior chapter. The magneto-optic Kerr effect studies were carried out in a different UHV instrument (with similar low base pressure) that also incorporates LEED and AES surface probes into a high-sensitivity magneto-optic Kerr effect polarimeter. This instrument was previously used in an experiment that probed for ferromagnetic ordering of p(1x1) V on Ag(100)^[78] and has also been described in other publications^[43].

Sample preparation and characterization of V(100) presented significant challenges^[79,80-83]. The first experiments in the 1980's to experimentally determine the surface structure of V(100)^[84] were carried out on a (5x1) reconstructed surface which was believed to be the clean vanadium surface. More recent studies of V(100) that combine high-resolution AES and scanning tunneling microscopy have shown that the (5x1) reconstruction is stabilized by low concentrations of oxygen (~0.2ML)^[74, 82]. When a low concentration of carbon is also present, it is possible to

detect spatial inhomogeneity of carbon and oxygen contamination, that manifests a superposition of $c(2 \times 2)$ and (5×1) diffraction patterns, by moving the primary LEED beam across the surface. The recent studies of adsorbates on V(100), including careful studies of hydrogen adsorption and desorption kinetics^[82] and the bulk/surface diffusion of C and O^[64], provide a useful body of knowledge for preparing and characterizing a “clean” V(100) surface.

Our V(100) crystal was prepared and cleaned using the same techniques developed and outlined for Nb(100) in the previous chapter. The crystal was cut from an aligned high-purity (99.99%) boule using a moving-wire electrode and aligned using x-ray Laue methods with the assistance of Orient Express^[11] software. During the initial cleaning cycles, AES detected near-surface contaminants of phosphorous, sulfur, carbon, and oxygen. Surface phosphorous and sulfur were depleted after about 80 hours of repeated sputtering and annealing to 1200K.

The final stage of sample cleaning requires removal of near-surface carbon and oxygen. Carbon segregation from the bulk to the surface occurs at 600K and carbon surface diffusion occurs at ~750K. Oxygen segregation to the surface occurs over the range of 600-950K, but oxygen absorbs into the bulk at higher temperature^[64]. The combination of bulk and surface diffusion of C and O and the high sticking probability of O and CO (and H) is the source of difficulty in obtaining a clean V(100) crystal surface. The problem is exacerbated by the near overlap of the primary oxygen AES peak (512 eV) with a prominent vanadium peak (510 eV). The peaks can be resolved by using a low ($< 2 V_{p-p}$) modulation voltage and slow energy

scan-rates when conduction AES. The following AES calibration results^[13, 30] were used to judge the concentration of C and O impurities on V(100): 1ML C corresponds to a C_{272}/V_{473} dN/dE peak ratio of 0.10; 1 ML of O corresponds to a O_{510}/V_{473} dN/dE peak ratio of 0.066 and a O_{492}/V_{473} dN/dE peak ratio of 0.022.

Final sample conditioning required over 1000 hours of sputtering, annealing, and flashing cycles following a procedure similar to that described by Jensen et al^[74]. The primary difference in our procedure was that neon was used as the sputtering gas. This permitted maintaining the titanium sublimation pump cryoshroud at 77°K (filled with LN₂) and permitted the LEED experiments to be carried out in the 8×10^{-11} Torr range. The sputtering, annealing (600-700K), and flashing to (1000K) finally resulted in a well-ordered (1x1) surface with O, P, and S contamination below the AES sensitivity limit (0.01 ML). Continuous use of the LN₂-cooled titanium sublimation pump during the final stages of sample conditioning and during measurements ensured CO and H partial pressure below 5×10^{-11} Torr and reduced the effects of surface contamination by residual gas to below 1-2% of a ML during the 40-min. period required to log LEED spectra.

The highest quality “clean” V(100) surface achieved in our experiments yielded AES spectra that indicated about 5% C ($C_{272}/V_{473} \cong .005$) and no other impurities at the sensitivity limit which was judged to be 1% for oxygen. The residual surface C was judged to originate from bulk diffusion during final annealing required to obtain a well-ordered surface and from CO contamination produced by tungsten filaments used during AES or LEED. The total surface contamination

determined by AES after a complete set of LEED IV spectra had been taken was typically 6-8%, and mostly C. The MOKE measurements were carried out at the lowest limit of C contamination ($\leq 5\%$).

VI.3 LEED Data and Analysis

LEED I-V data sets were acquired after symmetrizing conjugate (symmetry-degenerate) beam intensities in the usual manner: The orientation of the sample was adjusted until all conjugate beams yielded the same intensity. This process ensures normal incidence of the electron beam. Pendry r-factor analysis was used to characterize the internal consistency of the individual beams with their averages. The four-beam cumulative energy range is 1100-1200 eV, depending on the specific data set, which is adequate, based on prior studies^[7], to achieve convergence leading to an accurate structure determination. Typical r_p values for conjugate beam/averaged beam comparison of unsmoothed I-V spectra are: (10) beams (450 eV range) $r_p \sim 0.19$; (11) beams (350 eV range) $r_p \sim 0.038$; (20) beams (300 eV range) $r_p \sim 0.09$; (21) beams (200 eV range) $r_p \sim 0.085$.

We evaluated the compatibility of our data with relevant prior work (where I-V spectra were available) by digitizing the results of Jensen et al^[74] and conducting r-factor comparison of the averaged inequivalent beams with our unprocessed I-V spectra. Pendry r-factors comparing one of our room temperature I-V data sets (~ 1000 eV range, for nondegenerate beams) with the published Jensen et al data set^[15] yielded an averaged value $r_p \sim 0.45$. The agreement is not equivalent to the excellent agreement achieved by our group previously in corresponding comparisons

for Rh(100)^[57] and W(100)^[58]. For example in our comparison of an independently-measured Rh(100) data set, we obtained Zanazzi-Jona r-factors in the range $r_{zj} \sim 0.04$ -0.06; for W(100) a similar comparison yielded Pendry r-factors $r_p \sim 0.202$. Some of the (relatively large) differences between our (unsmoothed) I-V data and Jensen et al's data can be attributed to inaccuracies of digitizing the published spectra and the absence of any smoothing. Later, in discussing the extrapolation of LEED results to a clean surface value, it is shown that Jensen et al's surface structure results are compatible with other experiments taking into account estimated surface contamination and error estimates for the structure determination.

The Barbieri/Van Hove SATLEED code^[13] was used to numerically simulate the I-V spectra. A typical example is shown in Fig. 13 with a corresponding data set. The calculations were based on 13 relativistic phase shifts, which were also calculated using the Barbieri/Van Hove code. Convergence tests in which r-factors and structure parameters were evaluated as a function of the number of phase shifts used in the calculation revealed no differences for $l_{\max} \geq 6$. Standard r-factor analysis based on Pendry^[14] (r_p) and Zanazzi-Jona^[15] (r_{zj}) r-factors (also part of the SATLEED code package) was used to optimize structural and nonstructural parameters leading to structure determination based on measured I-V spectra.

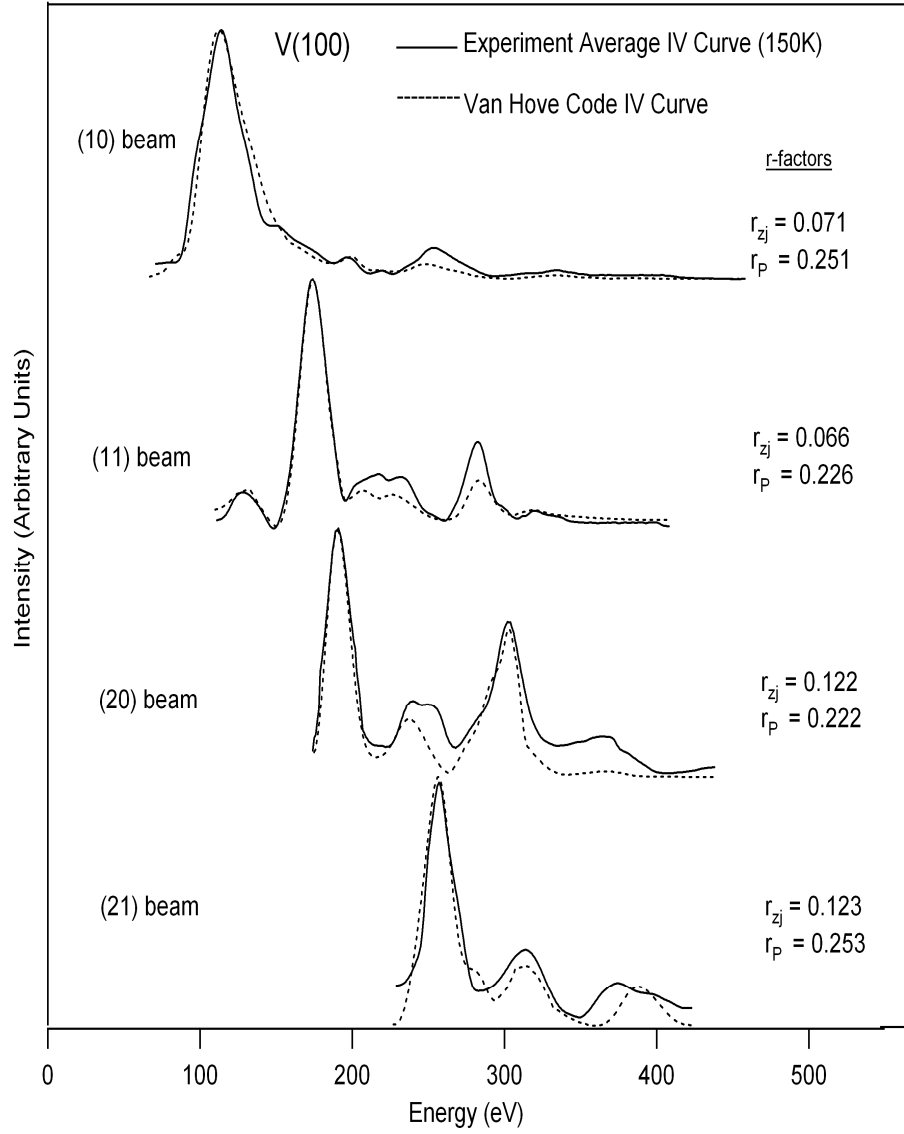


Figure 13. Representative LEED I-V data set for V(100) plotted with multiple-scattering simulations, and r-factors characterizing the precision of the experiment/calculated fit.

The structure search was initiated by setting nonstructural parameters near the optimized values determined by Jensen et al^[74] listed in Table IX. The imaginary part of the inner potential (inelastic scattering length) V_{im} was allowed to vary as part of the structure search for each data set. The structure search was restricted to

multilayer relaxation of surface atoms assumed to be in registry along the (100) surface normal direction. The range of parameter space searched was: d_{12} , 1.36-1.67 Å; d_{23} , 1.44-1.59 Å; and d_{34} , 1.50-1.53 Å (bulk value $d_0=1.514$ Å). The parameter V_{im} was varied in 1eV steps from -3eV to -9eV. The number of layers allowed to relax was varied from 1 to 4. Structure determinations were carried out using both “raw” and smoothed experimental I-V spectra. The raw I-V spectra produced slightly different values for nonstructural parameters and significantly larger r-factors than obtained from smoothed data, but the structural results obtained from smoothed and unsmoothed data sets differed very little (Fig. 13). Table IX summarizes the set of nonstructural and structural parameters that yielded the best three-parameter fits to 300K and 150K data sets.

VI.4 Results for Structure Search

Non-Structural Parameters	Data set		
	150K	300K	Jensen
Debye Temperature	380K	380K	510K
Vibrational Constant	1.4	1.4	--
Vibrational Symmetry	Isotropic	Isotropic	Isotropic
Inner Potential (Real, eV)	+8.0	+8.0	+9.2
Inner Potential (Imag., eV)	-5.0	-5.0	-4.0
Bulk Lattice Constant (Å)	1.514	1.514	1.514
Structural Parameter ($r_p=0.23$)			
$\Delta d_{12}(\%)$	-5.4 ± 2.5	-5.4 ± 2.5	-6.7 ± 1.5
$\Delta d_{23}(\%)$	$+2.5 \pm 2.5$	$+3.4 \pm 2.5$	$+1.0 \pm 1.3$
$\Delta d_{34}(\%)$	-1.8 ± 2.5	-1.4 ± 2.5	--

Table IX. Nonstructural parameters used in multiple-scattering structure searches and Δ_{ij} resulting from three-parameter fit to two LEED data sets. Two-parameter fit results for several data sets are displayed in Fig. 13. Results obtained by Jensen et al tabulated in right hand column.

Figure 13 displays experimental I-V spectra (measured at 150K) along with representative calculated spectra and the accompanying r-factors associated with the fit. Table IX summarizes the results of several structure searches based on various constraints imposed on structure variations. The total cumulative energy range covered by our V(100) I-V spectra is 1200eV. The Pendry r-factors for our V(100) structure determination exercises are comparable to corresponding values we obtained for W(110)^[7] (four-beam average $\langle r_p \rangle \sim 0.24$). The Zanazzi-Jona r-factors are comparable $\langle r_{zj} \rangle \sim 0.09$ for cumulative energy range of 1200 eV of the W(110)

data set. We note that Bergermeyer et al ^[33] (Table VIII) report values of Δ_{12} for V(100) with $r_p = 0.14$ (significantly better than the r_p values obtained in our study). The superior r-factor is consistent with the lower concentration of C ($\leq 4\%$) achieved in their “clean” V(100) surface which leads to lower impurity scattering in the LEED data (that is not accurately modeled in the structure search simulations). The effects of surface contamination on LEED structure determination of clean V(100) are discussed in more detail in the following section.

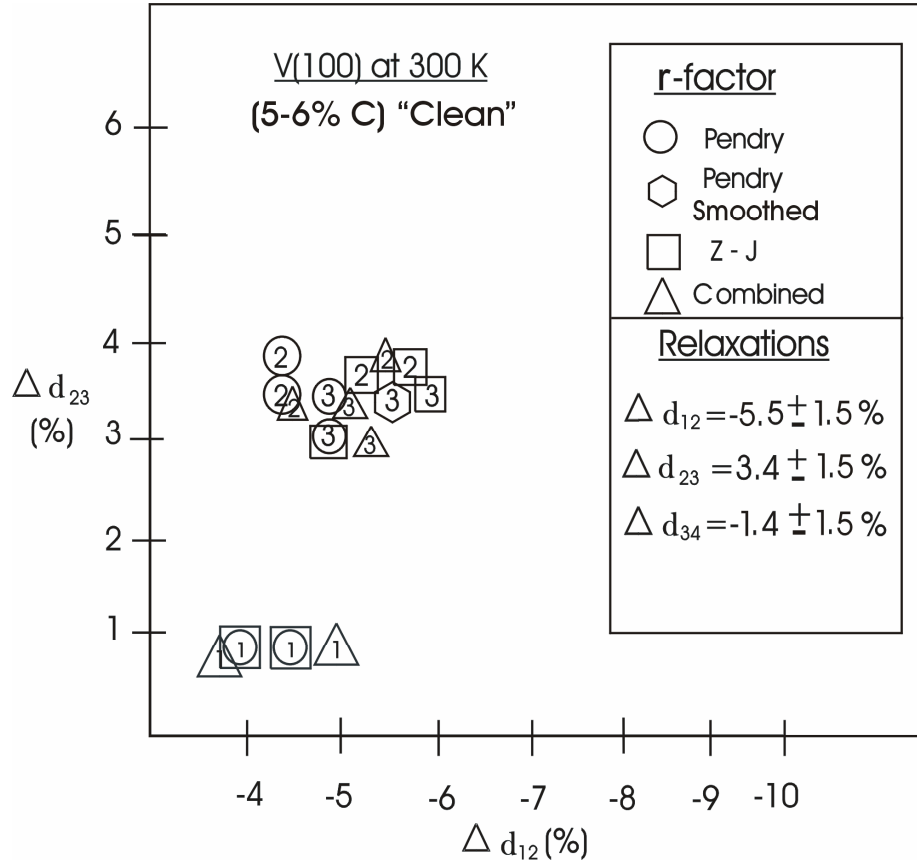


Figure 14. Graphical representation of variations in determined surface structure resulting from the use of different r-factors, from using smoothed and unsmoothed experimental 300K I-V spectra, and from using three different models. The number 1 inside a symbol indicates

a single-parameter fit (Δ_{12} only allowed to vary with Δ_{23} fixed at +1.0% and other Δ_{ij} held at bulk value); 2 indicates a two-parameter fit (Δ_{12} , Δ_{23}); and 3 indicates a three-parameter (Δ_{12} , Δ_{23} , Δ_{34}) fit. The indicated uncertainties in values of Δ_{ij} in the box reflect the convergence precision of the methodology. The structure accuracy (Table IX) is determined by considering the Pendry r-factor.

Several data sets were measured, and two of the data sets (one at 300K and one at 150K) were extensively evaluated based on several assumptions, including constraints on the number of layers allowed to relax, the type of r-factor used to determine the best fit, and, in some cases, restricting the analysis to three of the four nondegenerate beam spectra. The resulting values of d_{12} and d_{23} are presented graphically in Fig. 14. Based on these results, we obtain the following structural parameters for the multilayer relaxation of V(100): $\Delta d_{12} = -5.5 \pm 1.5\%$, $\Delta d_{23} = +3.39 \pm 1.5\%$, and $\Delta d_{34} = -1.4 \pm 1.0\%$ with typical surface C concentration ranging from 5% to 6% during the various measurements. The errors cited represent the convergence precision judged from the scatter of determined structure parameters based on different model constraints and r-factor criteria (Fig. 14). The accuracy of structure determination is discussed in the following section, and displayed in Fig. 15 for Δ_{12} as error bars.

VI.5 Surface Impurities and Structure Accuracy

Surface structure and magnetism are both strongly affected by chemisorbed atoms. Therefore, an important factor in using experimental results as a basis for judging the accuracy or validity of an ab-initio calculation is a realistic assessment of

surface impurity concentrations and their effects. The bulk purity of the boule from which a single-crystal sample is prepared can affect the ultimate limit of surface cleanliness achieved in sample preparation. The concentration of bulk carbon in vanadium appears to be the limiting factor in obtaining a clean V(100) surface. In our experiments, the lower limit of surface contamination (after over 1000 hours of sputtering and annealing) was 5% C. During LEED and AES experiments in which a tungsten filament was required as an electron source, this concentration would increase to as much as 8% (C + O) after about one hour. Similar results were reported by Koller et al^[83]. Bergermayer et al^[33] reported achieving C impurity levels of 4% in their LEED experiments; Jensen et al^[74] report extensive studies of oxygen contamination in their LEED experiments and state that C concentrations down to 0.05 monolayer (5%) were achieved. They also state that the measured coverage of CO after a set of LEED intensity measurements was below 0.1 monolayer, but clearly detectable using AES.

Bergermayer et al^[33] carried out extensive experimental (LEED and STM) and theoretical (ab-initio calculations) of c(2x2) and p(2x1) carbon on V(100). One specific result is an accurate determination of the structure of c(2x2) carbon on V(100). LEED intensity analysis and STM studies establish that c(2x2) C on V(100) occupies the hollow sites; and that at a surface concentration of $\Theta_c \sim 35\%$, that $\Delta_{12} = +4.6\%$. The c(2x2) C structure has been observed down to a surface concentration of 18%; below 10% C, the C layer is disordered and the “clean” V(100)

p(1x1) structure is observed. These results combined with the structure parameters for V(100) from Table VIII, and our additional LEED structure analysis of V(100) surfaces having higher carbon concentrations than 5% yield the results displayed in Fig. 15. This figure illustrates the experimentally-determined relationship between Δ_{12} and surface carbon contamination established by LEED crystallography using the previously-stated AES calibration criteria.

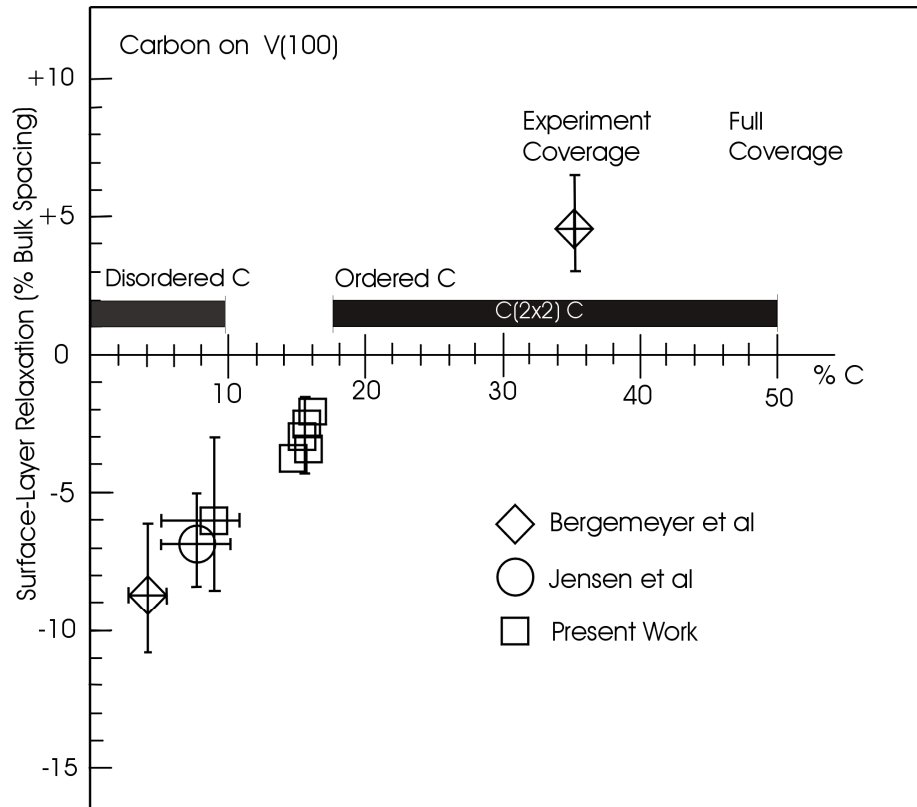


Figure 15. Values of first-layer relaxation Δ_{12} at V(100) determined by LEED as a function of surface carbon contamination. Carbon concentrations are based uniformly on AES dN/dE calibrations^[33, 64] stated in text ($C_{272}/V_{473} = 0.10$ for 1 ML carbon), and on AES spectra or surface C concentration stated in the cited papers. Error bars on carbon concentration for present work represents the (5-8%) range of measured C concentrations for all LEED experiments. Error bars on

accuracy of Δ_{12} for present work are based on the Pendry r-factor (Table VII)

Theoretical models of chemisorption^[68] (as well as experiments) have shown that surface parameters such as the workfunction, top-layer relaxation and the repulsive adsorbate-adsorbate interaction that leads to ordered overlayer structures, all of which originate from charge transfer associated with chemisorption, scale linearly with adsorbate concentration for low coverages ($\Theta < 0.1\text{ML}$). It is therefore reasonable to use a linear model to extrapolate measured first-layer relaxation as a function of measured C concentration to the clean surface value. The extrapolation suggests that a realistic clean surface value of d_{12} and Δ_{12} for V(100) to use in judging the validity of an ab-initio calculation is $d_{12} = 1.36 \pm 0.05\text{\AA}$, corresponding to a contraction of $\Delta_{12} \sim 10 \pm 3\%$ relative to the bulk spacing $d_0 = 1.514\text{\AA}$. The linear extrapolation appears to extend to the (positive) relaxation for c(2x2) C on V(100) at the experimentally-determined average surface concentration of $\Theta_c \sim 35\%$ (a coverage significantly beyond the range where a linear extrapolation is expected to be valid).

VI.6 Probe for Surface Magnetism at V(100)

We have reported prior experimental attempts to detect ferromagnetism in p(1 x 1) Rh on Ag(100) and p(1 x 1) V on Ag(100)^[78] based on the magneto-optic Kerr effect (MOKE). The same instrument^[43] was used to prepare and characterize the “clean” V(100) surface and carry out an in-situ probe for magnetism using the MOKE. The sensitivity of the polarimeter has been improved by replacing the He Ne

laser with a solid state laser. The sensitivity limit achieved in our experiment is discussed below in relation to the expected magneto-optic effects from a magnetic V(100) surface based on layer-dependent magnetic moments predicted by ab-initio calculations^[38].

Prior experiments on epitaxial Fe on Ag(100)^[85], where the Fe magnetic moment $\mu \cong 2.2\mu_B$ per atom, have shown that typical MOKE rotations and ellipticities of ultrathin films and superlattices are proportional to the film thickness and magnetization, and are of the order of 0.007 mrad/monolayer. In a prior experiment^[78], it was shown that a hysteresis loop produced by a 2 ML Fe film on Ag(100) can be integrated to a signal-to-noise ratio of over 100:1 in approximately 100 sec, corresponding to a polarimeter sensitivity of $\sim 0.1 \mu\text{rad}$ and a magnetic moment detection sensitivity of less than $0.2 \mu_B$ per surface atom.

The polarimeter calibration experiment, displayed in Fig. 16, demonstrates higher sensitivity. The sensitivity was determined by placing a Faraday cell in the optical path between the polarizer and the V(100) sample. The cell consisted of a 1 mm thick glass slide (Verdet constant $V \cong 15 \times 10^{-3} \text{ min/Oe cm}$) and a current-carrying coil having its axis along the optical path. This Faraday cell produced rotations of approximately $0.50 \mu\text{rad/Oe}$. The optical quality of the polished bulk crystal V(100) surface after in-situ cleaning is not quite equivalent to that of a commercially-prepared growth substrate (silicon or sapphire, for example), and some loss in polarimeter sensitivity resulting from light-scattering and depolarization

effects is expected. Replacement of the 3 mW HeNe laser used in prior experiments by a 30 mW solid state laser has compensated for the reduction in sensitivity associated with the less-than-ideal optical quality of the bulk V(100) surface. The overall sensitivity of the polarimeter is estimated to be a factor of four better than the prior reported value obtained using films on high-quality optical substrates, and slightly better than achieved in the study of V and Rh films grown on Ag(100). After 100 seconds of integration, $\pm 1.0 \mu\text{rad}$ rotation can be measured to a signal-to-noise ratio exceeding 10:1. (Corresponding to a sensitivity exceeding $0.05 \mu\text{rad}$).

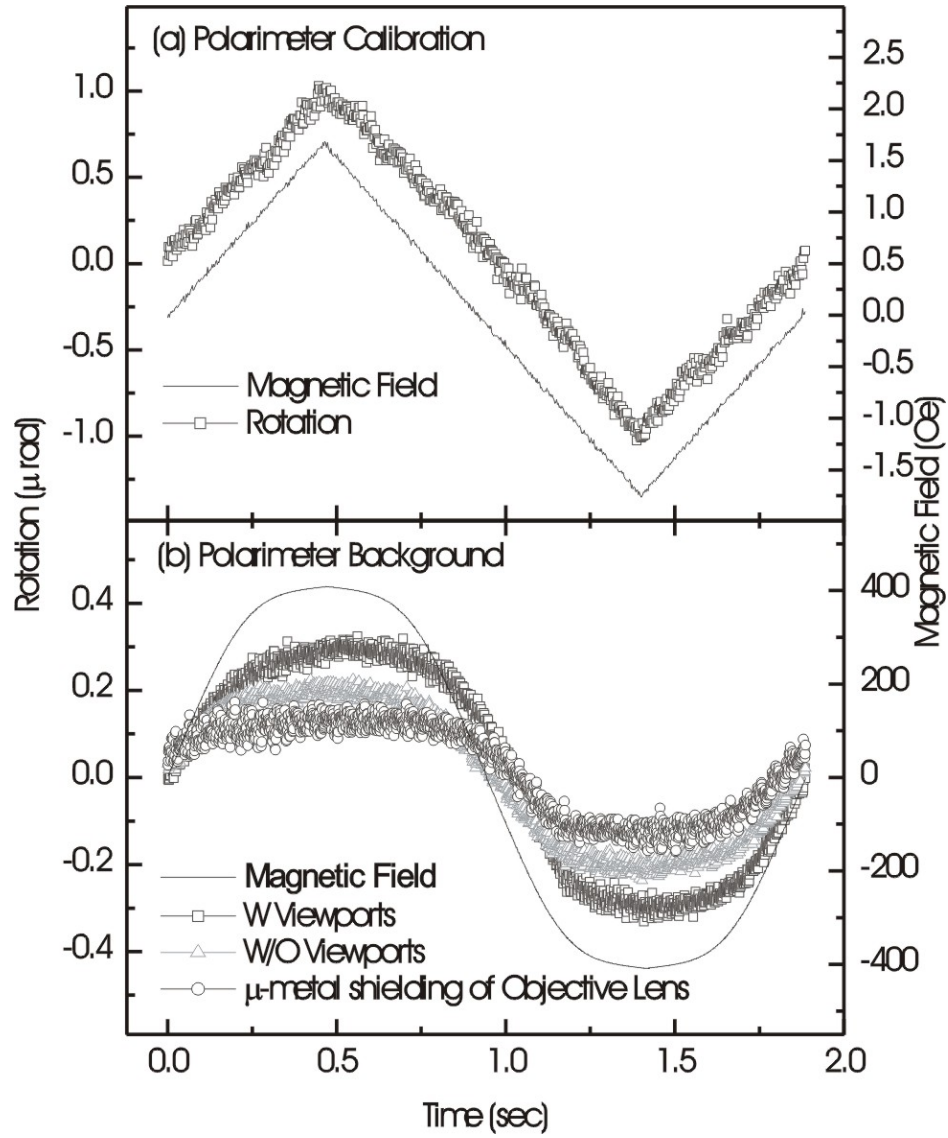


Figure 16. Upper panel, sensitivity evaluation and calibration of polarimeter based on Faraday cell showing detected rotation of 1 μrad (from triangle wave applied field) with sensitivity corresponding to a signal-to-noise ratio of 20:1.

Lower panel, evaluation of background detected signals from stray fields interacting with viewports and optics. The V(100) crystal is replaced by a (non magnetic) gold mirror.

An estimate of the expected Kerr signal can be obtained from the ab-initio calculations of the layer-dependent magnetic moment at V(100)^[36]. In the favorable case (surface relaxation of ~6% corresponding to measured values at typical C concentrations in our LEED experiments), the first-layer magnetic moment in units of Bohr magnetons is +1.452, with subsequent layer moments of -0.698, -0.352, and -0.149. The net calculated moment for the top four layers is $0.253\mu_B$. A more elaborate (but not necessarily better) estimate that includes effects of optical penetration $\delta \sim 200\text{\AA}$ and assumes that the moments in surface layers after $n = 4$ continue the trend of the second, third, and fourth layer (reduction of each following layer moment by factor of two) yields a net moment of $\mu_{\text{net}} = 0.194 \mu_B$. It is reasonable to assume for magnetic V(100) that the MOKE signal will be equivalent to that produced by a one monolayer ferromagnetic film having a magnetic moment of $0.2 \mu_B$ (corresponding to a MOKE rotation of $0.65 \mu\text{rad}$). This assumption is strengthened by the fact that ab-initio calculations^[36, 38] attribute a significant fraction of the net V(100) surface magnetic moment to a surface state. Other factors, including spin-orbit coupling strength and optical matrix element weight at the laser wavelength, are assumed equivalent to other metallic ferromagnets (i.e. Fe), which appears to be reasonable.

Measurements of the magnetic moment of V(100) using the Magneto Optic Kerr Effect were largely performed by Jusang Yang. Surface magnetism at V(100) was probed using the MOKE technique to an estimated sensitivity exceeding

$0.05\mu_B/\text{atom}$ as described in Fig. 16. These conditions require integration of the detected MOKE signal to an equivalent Kerr rotation of less than $0.05\mu\text{rad}$ at a S/N ratio of 1:1. At this sensitivity, the Faraday rotation produced by the stray-field component of the electromagnet (along the beam axis) interacting with vacuum view ports was easily observed. Consistency tests verified that the detected signal from V(100) (Fig. 17) in phase with the drive-field was proportional to the stray magnetic field and was associated with the optical viewports not with the V(100) surface. The range of parameters (applied field to 450 Oe, temperature 150-300K, and surface contamination < 0.05 ML of O, C) covered the range of parameters reported in the electron-capture-spectroscopy experiment^[41]. Our MOKE experiments failed to detect evidence of a ferromagnetic V(100) surface at the sensitivity limit of $0.05 \mu_B/\text{surface atom}$.

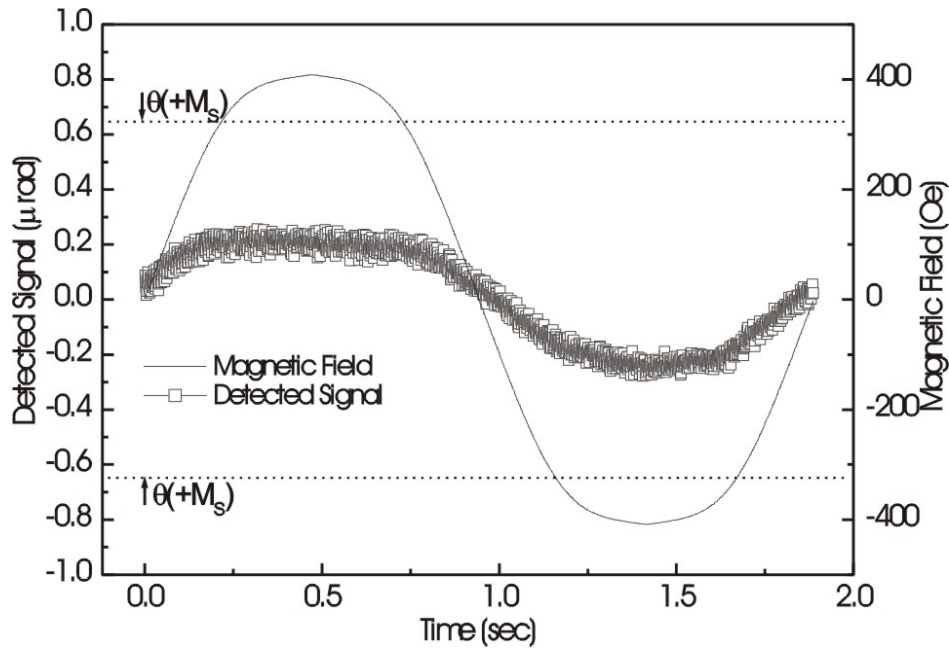


Figure 17. Detected signal with 400 Oe peak-to-peak magnetic field applied to V(100). Systematic checks (refers to text and Fig. 16) show that the signal is produced by stray fields from the electromagnet that produce Faraday rotation in the vacuum viewports. Any signal produced by the V(100) surface is below the detection limit ($\Theta < 0.05 \mu\text{rad}$). Dotted lines show amplitude of signal based on ab-initio calculations (refer to text).

VI.7 Conclusions

Experiments that probe the surface structure and search for surface magnetism at V(100) are described. The results are discussed in relation to experimental limitations of preparing a perfectly clean surface and in relation to density functional calculations. Bulk carbon in V appears to restrict surface sensitive experiments on V(100) to a practical lower limit of 4-5% carbon concentration. LEED intensity measurements on V(100) with calibrated C surface concentrations below 10% combined with existing published LEED results are used to obtain a meaningful extrapolation of first-layer relaxation of V(100) to a clean surface value: $d_{12} = 1.36 \pm 0.05 \text{\AA}$ corresponding to a contraction of a $10 \pm 3\%$ relative to the bulk lattice spacing. A high sensitivity probe for surface magnetism on technically-clean ($C < 5\%$) V(100) failed to detect any evidence of surface magnetism at V(100). The sensitivity of the experiment is estimated to be $0.05 \mu_B$ per surface atom, and the experiment covers the parameter space described in the prior electron-capture spectroscopy experiment^[41] that reported ferromagnetic order. It is important to note that the MOKE probes the net magnetic moment averaged over the optical penetration depth (few hundred \AA) whereas electron-capture is sensitive only to the surface magnetic moment, and

particularly sensitive to a magnetic surface state. In principle, the electron-capture experiment is more sensitive to surface magnetism, and represents a more direct probe in the sense that spin polarization is measured. MOKE rotations are indirectly related to spin polarization through spin-orbit coupling and optical matrix element strengths. Nevertheless, the sensitivity ($0.05 \mu_B/\text{atom}$) of our probe for magnetic order at V(100) should be considered a valid indication that the surface of V(100) is not ferromagnetic.

In relation to the large number of results from ab-initio calculations for V(100), it is clear that our extrapolated experimental value of top-layer relaxation (to a clean surface value $\Delta_{12} \sim -10\%$) is in good agreement with the typical calculated values. The absence of (or very small) surface magnetic moment at V(100) favors all-electron approaches over pseudopotential approaches in computing magnetic behavior based on ab-initio methods.

VII Conclusion

Low Energy Electron Diffraction intensity measurements and multiple scattering analysis have been used to determine the multilayer relaxation of three surfaces as a function of temperature: clean V(100), clean Nb(100), and hydrogen-dosed Nb(100). Accurate characterization of residual surface impurity concentrations (carbon, oxygen) based on Auger electron spectroscopy was used to obtain a meaningful extrapolation of the first-layer relaxations to the clean surface values.

Table X presents a survey of experimental and theoretical first layer relaxation results for Feibelman-issue transition metals including current (extrapolated V(100) and Nb(100)) and previously-studied (Rh(100), W(110), and Ti(0001)) surfaces. The extrapolated values corroborate independent published experimental results and theoretical predictions. Our experimental results for d_{12} were used to judge the accuracy of recent ab-initio calculations for V(100) and Nb(100). Our research shows that small concentrations of surface impurities can have a significant affect on surface layer relaxations, and are the primary cause of the Feibelman issue for Vanadium and Niobium. By accounting for the surface impurities for both of these surfaces, the Feibelman issue discrepancy for V(100) and Nb(100) has been resolved.

Temperature-dependent changes in surface relaxation resulting from hydrogen dosing of Nb(100) manifest an expansion of the near-surface lattice resulting from subsurface hydrogen atoms. The hydrogen-induced expansion of near-surface interplanar separation was determined to be $3 \pm 1\%$ at $T = 125\text{K}$, $4 \pm 1\%$ at $T = 300\text{K}$,

and $-1 \pm 1\%$ at $T = 400\text{K}$. The observed relaxation of the hydrogen-dosed near-surface interplanar separation to the clean surface value for $T > 400\text{K}$ is consistent with the subsurface “hydrogen valve” model that has been used to account for unusual hydrogen uptake kinetics associated with Nb(100).

A high-sensitivity probe for surface magnetism based on magneto-optic Kerr effect polarimetry using the cleanest V(100) surfaces achieved during the LEED experiment ($\sim 5\%$ C) yielded a (sensitivity-limited) null result with an estimated upper limit of $0.05 \mu_B/\text{surface atom}$. These results were discussed in relation to the predictive accuracy of ab-initio calculations that explored the surface structure and magnetism of V(100).

Future work on the Feibelman issue includes a project that will map the first interstitial layer as a function of the workfunction in order to further validate the extrapolation scheme employed during the LEED analysis outlined in Chapters 5 and 6. Continued LEED IV measurements of unstudied transition metals, such as Re(1000) and selected rare-earth metals including Gd, will be performed to resolve experiment-theory discrepancies. Our group will continue to measure the effect of surface hydrogen on structural relaxations through hydrogen dosing experiments using a transition metal with surface reconstructions. Our research involving niobium will continue with angle resolved photoemission experiments of carried out at low temperatures in an effort to conclusively resolve the dispute surrounding the uptake processes of hydrogen.

$\Delta d_{12}/d_0$		
Surface	Experiment	Theory
<i>Ti(0001)</i>	-4.9%	-6.8%, -7.7%
Zr(0001)	-1%, -1.6%	-4.4%, -6.3%
Mo(110)	-1.6%	-3.9%, -4.5%
<i>Rh(001)</i>	-1.4%	-1.4%, -3.5%
Ru(0001)	-2.0%	-4%
<i>W(110)</i>	-3.0%	-3.6%
Nb(100)	-10%*, -13.5%	-11.65%, -12.1%
V(100)	-8.6%, -10%*	-11.1%, -12.5%

Table X. Summary of Surface Relaxations studies for transition metals with Feibelman issue discrepancies. Experimental numbers with an asterisk indicate the extrapolated relaxation values of the current research. Experimental numbers in italics were resolved through previous research performed by G. Teeter.

Bibliography

1. Glenn Teeter, Surface Relaxation Studies of Clean Metal Surfaces, Doctoral Dissertation, University of Texas at Austin, 1999.
2. Don Hinson, Development of a Low Energy Electron Diffraction Data-Taking System, and the Determination of Rh(100) and W(100) Surface Relaxations by LEED, Doctoral Dissertation, University of Texas at Austin, 1997.
3. P.J. Feibelman, Surf. Sci. 360, 297(1996)
4. P.J. Feibelman, Phys. Rev. B 53, 13740(1996)
5. C.L.Hedberg ed., *Handbook of Auger Electron Spectroscopy*, Physical Electronics, Inc., 1995
6. G. Teeter, D. Hinson, J. L. Erskine, C. B. Duke, and A. Paton, *Phys. Rev. B* 57, 4073 (1998).
7. G. Teeter, J. L. Erskine, F. Shi, and M. A. Van Hove, *Phys. Rev. B* 60, 1975 (1999).
8. G. Teeter and J. L. Erskine, *Phys. Rev. B* 61, 13,929 (2000).
9. Y. Margoninski, *Contemporary Physics*, 27, 203 (1986)
10. A. Zangwill, *Physics at Surfaces*, Cambridge University Press, 1988.
11. OrientExpress. J. Laugier and Associates. <http://www.ccp14.ac.uk/ccp/web-mirrors/lmgp-laugier-bochu>
12. David Lacina, "Crystal Preparation and Low Energy Electron Diffraction Studies of V(100)", Masters Thesis, University of Texas at Austin, 2004.

13. A. Barbieri/M. A. VanHove, Automated Tensor LEED Program, available from M. A. VanHove at Lawrence Berkeley Laboratory.
14. J.B. Pendry: J. Phys. C 13, 937 (1980).
15. E. Zanazzi, F. Jona: Surface Science, 62, 61 (1977).
16. M.W. Finnis, V. Heine, J. Phys. F 4, L37(1974)
17. R. Smoluchowski, Phys. Rev. 60, 661(1941)
18. S.P. Chen, Surf. Sci. Lett. 264, L162(1992)
19. E.W. Plummer, P.T. Sprunger, et al., Surf. Sci. Lett. 297, L48(1993)
20. E.W. Plummer, H.L. Davis, et al., Phys. Rev. Lett. 68, 2632(1992)
21. E.W. Plummer, P. Hofmann, et al., Phys. Rev. B 53,13715(1996)
22. A. Kiejna, *Surface Science*, 598, 276(2005)
23. M.A. Pick, J.W. Davenport, M. Strongin, and G. Dienes, *Phys. Rev. Lett.* 43, 286(1979).
24. R. J. Smith, *Phys. Rev. Lett.* 45, 1277 (1980).
25. M. Strongin, J. Colbert, G. Dienes, and D. Welch, *Phys. Rev.* B26, 2715(1982)
26. B. –S. Fang, C. A. Ballentine, and J. L. Erskine, *Surface Science* 204, L713 (1988).
27. M. Lagos, I.K. Schuller, *Surface Science Lett.* 138, L161(1984).
28. M. Lagos, J. Rogan, and I. K. Schuller, *Phys. Rev.* B44, 3380 (1991).
29. M. Lagos, G. Martinez, and I. Schuller, *Phys. Rev.* B29, 5979(1984)
30. B. –S. Fang, C. A. Ballentine, and J. L. Erskine, *Phys. Rev.* B38, 4299 (1988).

31. B. –S. Fang, C. A. Ballentine, and J. L. Erskine, *Phys. Rev.* B36, 7360 (1987).
32. H. Akoh , and A. Tasaki, *J. Phys. Soc. Jpn.* 42, 791 (1977).
33. W. Bergermayer, R. Koller, C. Knovicka, M. Schmid, G. Kresse, J. Redinger, P. Varga, and P. Podloncky, *Surf. Sci.* 497, 294 (2002).
34. I. Turek, S. Blügel, and J. Kudrnovsky, *Phys. Rev.* B57, 11,065 (1998).
35. S. Ohnishi, C. L. Fu, and A. J. Freeman, *J. Magn. Magn. Mater.* 50, 161 (1985).
36. I. Batyrev, J. –H. Cho, and L. Kleinman, *Phys. Rev. B* 63, 172420-1 (2001).
37. G.Bihlmayer, T. Asada, and S. Blügel, *Phys. Rev. B* 62, R11,937 (2000).
38. T. Bryk, D. M. Bylander, and L. Kleinman, *Phys. Rev. B* 61, R3780 (2000).
39. R. Robles, J. Izquierdo, A. Vega, And L. C. Balbas, *Phys. Rev.* B63, 172406-1 (2001).
40. M. M. J. Bischoff, C. Knovicka, A. J. Quinn, M. Schmid, J. Rediger, R. Podlouncky, P. Varga, and H. van Kempen, *Phys. Rev. Lett.* 86, 2396 (2001).
41. C. Rau, C. Liu, A. Schmalzbauer, and G. Xing, *Phys. Rev. Lett.* 57. 2311 (1986).
42. C. Rau, G. Xing, and M. Robert, *J. Vac. Technol.* A6, 579 (1988).
43. C. A. Ballentine, R. L. Fink, J. Araya-Pochet, and J. L. Erskine, *Appl. Phys.* A49, 459 (1989).
44. S. Blügel, D. Drittler, R. Zeller, and P. H. Dederichs, *appl. Phys. A Solids Surf.* A49, 547 (1989).

45. N. Shamir, U. Atzmony, J. A. Schultz, and M. H. Mints, *J. Vac. Sci. Technol.* A5, 1024 (1987).
46. T. E. Felter, R. A. Barker, and P. J. Estrup, *Phys. Rev. Lett.* 38, 1138 (1977).
47. S. -W. Kim and K. -S. Sohn, *Phys. Rev.* B40, 1003 (1989).
48. M. Lagos and I. K. Schuller, *Phys. Rev.* B32, 5477 (1985).
49. G. J. Dienes, M. Strongin, and D. O. Welch, *Phys. Rev.* B32, 5475 (1985).
50. W. Eberhardt, F. Greuter, and E. W. Plummer, *Phys. Rev. Lett.* 46, 1085 (1981).
51. B. -S. Fang, W. -S. Lo, and H. H. Chen, *Phys. Rev.* B47, 10,671 (1993).
52. B. -S. Fang, W. -S. Lo, T. -S. Chien, T. C. Leung, C. Y. Lue, C. T. Chan, and K. M. Ho, *Phys. Rev.* B50, 11093 (1994).
53. Y. Li, J. L. Erskine, and A. C. Diebold, *Phys. Rev.* B34, 5951 (1986).
54. E. Hulpke, M. Hüppauff, D. -M. Smilgies, A. D. Kulkarni, and F. W. deWette, *Phys. Rev.* B45, 1820 (1992).
55. W. -S. Lo, T. -S. Chien, B. -S. Fang, C. M. Wei, and W. N. Mei, *Surf. Rev. and Letters* 5, 1035 (1998).
56. A.R. Jani, N. E. Brener, and J. Callaway, *Phys. Rev.* B38, 9425 (1988).
57. K. -M. Ho, H. -J Tao, and X. -Y. Zhu, *Phys. Rev. Lett.* 53, 1586 (1986).
58. J. S. Luo and B. Legrand, *Phys. Rev.* B38, 1728 (1988).
59. M. Methfessel, D. Hennig, and M. Schaeffler, *Phys. Rev.* B46, 4816 (1992).
60. M. Brejnak and P. Modrak, *Surf. Science* 310, L614 (1999).

61. Ch. E. Lekka, M. J. Mehl, N. Bernstein, and D. A. Papaconstantopoulos, *Phys. Rev. B* 68, 035422 (2003).
62. D. Lacina, J. Yang, and J. L. Erskine, *Phys. Rev. B* 75, 195432 (2007).
63. B. An, S. Fukuyama, K. Yokogawa, and M. Yoshimura, *Phys. Rev. B* 68, 115423 (2003).
64. M. Beutl, J. Lesnik, E. Lundgren, C. Knovicka, P. Varga, and K. D. Rendulic, *Surf. Sci.* 447, 245 (2000).
65. W. Eberhard and E. W. Plummer, *Advances in Chemical Physics*, 49, 533-656 (1982).
66. F. J. Himpsel and W. Eberhard, *Physical Review Letters*, 42, 1375 (1979).
67. J.W. Davenport, G. Dienes, and R. Johnson, *Phys. Rev. B* 25, 2165(1982).
68. M. Scheffler and C. Stampfl, *Handbook of Surface Science* v. 2, K. Horn and M. Scheffler eds. Elsevier, Amsterdam (1999).
69. T. G. Walker and H. Hopster, *Phys. Rev. B* 49, 7687 (1994).
70. P. Fuchs, K. Totland, and M. Landolt, *Phys. Rev. B* 53, 9123 (1996).
71. M. Finazzia, P. Bencok, H. Hricovini, , F. Chevrier, E. Kolb, G. Krill, M. Vesely, C. Chappert, and J.-P. Renard, *Thin Solid Films*, 317, 314 (1998).
72. G. R. Harp, S. S. Parkin, W. L. O'Brien, and B. P. Tonner, *Phys. Rev. B* 51, 3293 (1995).
73. M. M. Schwickert, R. Coehoorn, M. A. Tomaz, E. Mayo, D. Lederman, W. L. O'Brien, T. Lin, and G. R. Harp, *Phys. Rev. B* 57, 13,681 (1998).

74. V. Jensen, J.N. Anderson, H.B. Nielson, and D.L. Adams, *Surface Science* 116, 66 (1982)
75. G. Teeter and J. L. Erskine, *Surface Review Lett.* 6, 813 (1999).
76. F. Jona, *Surface Science* 192, A569 (1987).
77. P. M. Marcus, P. Jiang and F. Jona, *Surface Science* 192, A569 (1987).
78. R. L. Fink, C. A. Ballentine, J. L. Erskine, and J. A. Araya-pochet, *Phys. Rev. B* 41, 10,175 (1990).
79. F. Dulot, P. Turban, B. Kierren, J. Eugène, M. Alnot, and S. Andrieu, *Surface Science* 473, 172 (2001).
80. G. Krenn, C. Eibl, W. Mauritsch, E. L. D. Hebenstreit, P. Varga, and A. Winkler, *Surface Science* 445, 343 (2000).
81. J. S. Foord, A. P. C. Reed, and R. M. Lambert, *Surface Science* 129, 79 (1983).
82. M. Kralj, P. Pervan, M. Milun, K. Wandelt, D. Mandrino, and M. Jenko, *Surface Science* 526, 166 (2003).
83. R. Koller, W. Bergermayer, G. Kresse, E. L. D. Hebenstreit, C. Konvicka, M. Schmid, R. Podloucky, and P. Varga, *Surf. Science* 480, 11 (2001).
84. P.W. Davies and R.M. Lambert, *Surface Science*, 107, 391 (1981).
85. S. D. Bader and J. L. Erskine, "Magnetism in Ultrathin Films," Editors, B. Henrich and J. A. C. Bland (Springer-Verlag, Berlin, 1994) Page 297.
86. W. Oed, B. Dotsch, L. Hammer, and K. Muller, *Surf. Sci.* 207, 55 (1988).
87. A.M. Begley, F. Jona, and P.M. Marcus, *Phys. Rev. B* 48, 12326 (1993)

Vita

David Glenn Lacina was born in McAllen, Texas on July 8, 1977, the son of Glenn and Florence Lacina. After graduating from McAllen Memorial High School in McAllen, Texas in May 1995, he entered Texas Tech University during August of that same year. He graduated in May 1999 and received a Bachelor of Science degree. In September 1999, he entered the Graduate School of The University of Texas and received a Masters of Science in Applied Physics degree in December 2002. In March of 2003, he passed the qualifying exam and was accepted into the doctoral program in the physics department.

Permanent Address: 1071 Clayton Ln #1532, Austin, Texas, 78723

This dissertation was typed by the author